Article

De novo design of transmembrane fluorescence-activating proteins

https://doi.org/10.1038/s41586-025-08598-8

Received: 26 September 2023

Accepted: 9 December 2024

Published online: 19 February 2025

Check for updates

Jingyi Zhu[1,2,3,4,5], Mingfu Liang[1,2,3,4,5], Ke Sun[2,3,4,5], Yu Wei[2,3,4], Ruiying Guo[2,3,4], Lijing Zhang[2,3,4], Junhui Shi[2,3,4], Dan Ma[2,3,4], Qi Hu[2,3,4], Gaoxingyu Huang[2,3,4] & Peilong Lu[2,3,4]✉

The recognition of ligands by transmembrane proteins is essential for the exchange of materials, energy and information across biological membranes. Progress has been made in the de novo design of transmembrane proteins[1–6], as well as in designing water-soluble proteins to bind small molecules[7–12], but de novo design of transmembrane proteins that tightly and specifically bind to small molecules remains an outstanding challenge[13]. Here we present the accurate design of ligand-binding transmembrane proteins by integrating deep learning and energy-based methods. We designed pre-organized ligand-binding pockets in high-quality four-helix backbones for a fluorogenic ligand, and generated a transmembrane span using gradient-guided hallucination. The designer transmembrane proteins specifically activated fluorescence of the target fluorophore with mid-nanomolar affinity, exhibiting higher brightness and quantum yield compared to those of enhanced green fluorescent protein. These proteins were highly active in the membrane fraction of live bacterial and eukaryotic cells following expression. The crystal and cryogenic electron microscopy structures of the designer protein–ligand complexes were very close to the structures of the design models. We showed that the interactions between ligands and transmembrane proteins within the membrane can be accurately designed. Our work paves the way for the creation of new functional transmembrane proteins, with a wide range of applications including imaging, ligand sensing and membrane transport.

Transmembrane proteins are integral components of cellular membranes, providing pathways for communication and transport between compartments separated by the lipid bilayer. Understanding the interaction between transmembrane proteins and small molecules is crucial for a wide range of biological processes, and holds great potential for developing genetically encoded tools. However, the variety of known natural transmembrane protein folds and their ligands is highly limited, and the design of ligand recognition by de novo transmembrane protein has so far been limited to haeme-binding through iron–histidine coordination[14–16]. This type of covalent interaction is well defined in naturally existing proteins, and the three-dimensional structures of these designs have yet to be determined. So far, there is no de novo-designed transmembrane protein that specifically binds to a given small molecule through non-covalent interactions.

The recent development of deep learning-based methods has substantially improved the accuracy of protein structure prediction[17–19]. Furthermore, substantial progress has been made in adapting deep networks for protein design, leading to improved success rates in various design tasks, such as sequence design, backbone generation and functional site scaffolding[20–24]. Although breakthroughs have been made to design pockets within closed repeat proteins[25] and pseudocycles[12], as well as to generate scaffolds for luciferase activity centres[26] and design ligand–protein interactions[27], the extension of design principles for soluble ligand-binding proteins to transmembrane proteins has yet to be explored. To our knowledge, very limited previous research has investigated the capability of deep neural networks to generate sequences for transmembrane proteins, or to scaffold functional motifs within membranes.

Here we report the accurate de novo design of highly active ligand-binding transmembrane proteins by integrating deep learning methods with energy-based methods. We used a two-step protocol in which we initially designed a stable, water-soluble fluorescence-activating protein (wFAP), followed by the creation of the transmembrane form (tmFAP) through resurfacing of membrane-embedded residues. We focused on designing α-helical transmembrane proteins, as non-toxic β-barrel transmembrane proteins tend to localize to the outer membranes of prokaryotic cells, mitochondria and chloroplasts[28].

Design of wFAP

In the first step of our design protocol, we aimed to design water-soluble protein sequences that adopt a stable four-helix bundle conformation, featuring a central pocket that exhibits favourable interactions to bind and activate fluorogenic (4-((2-hydroxyethyl)(methyl)amino)-benzylidene)-cyanophenyl-acetonitrile (HBC) derivatives[29] (Fig. 1a and

[1]College of Life Sciences, Zhejiang University, Hangzhou, China. [2]Westlake Laboratory of Life Sciences and Biomedicine, Hangzhou, China. [3]Research Center for Industries of the Future, School of Life Sciences, Westlake University, Hangzhou, China. [4]Institute of Biology, Westlake Institute for Advanced Study, Hangzhou, China. [5]These authors contributed equally: Jingyi Zhu, Mingfu Liang, Ke Sun. ✉e-mail: lupeilong@westlake.edu.cn

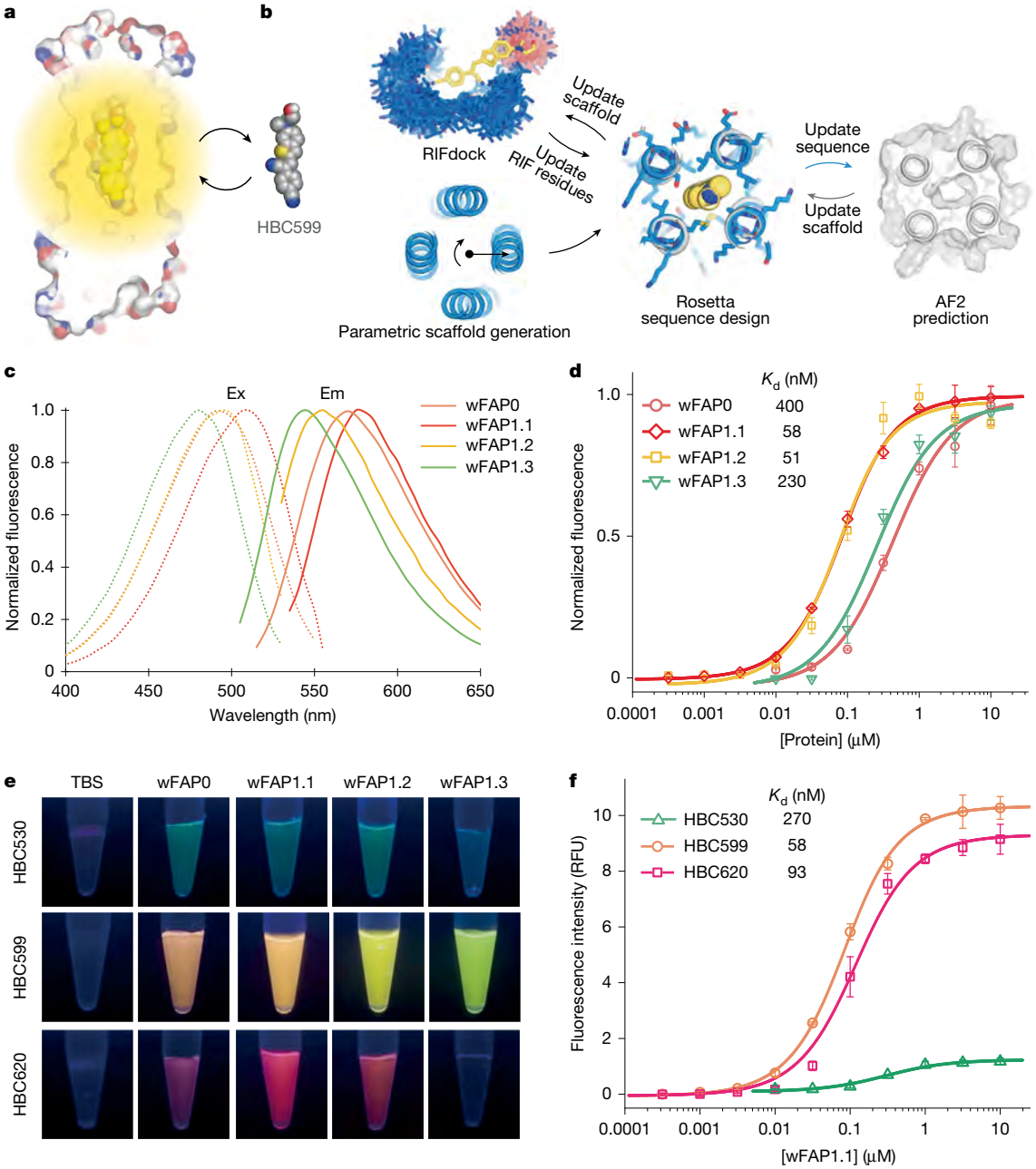

Fig. 1 | Design and characterization of wFAPs. a, Schematic illustration of the fluorescence activation mechanism of FAPs. The fluorogenic HBC ligands fluoresce only when bound to certain molecules, such as FAPs, that constrict them to a planar conformation. **b**, Design approach for wFAPs. Upper left: generated RIF for HBC599. The ligand was then docked to parametrically generated helical scaffolds (lower left) by RIFdock. While keeping the RIF residues fixed, the protein sequence was designed by Rosetta (middle). After sequence design and filtering, backbone coordinates were constrained to the AF2 model (white) for the next round of sequence design. The process was iterated to allow communication between the energy-based modelling and AF2 network (arrows between middle and right). High-quality backbones generated during iterations were used as additional input to RIF, for a more diverse set of outputs (arrows between upper left and middle). Output sequences were selected from converged iterations in which the Rosetta design model agreed with AF2 predictions. **c**, Excitation (Ex) and emission (Em) spectra of the wFAP variants complexed with the HBC599 fluorophore. **d**, Dissociation constant (K_d) determined by titrating purified wFAPs against 50 nM HBC599 (see Methods for details on fitting). Data from three experiments are presented as mean ± s.d. **e**, Fluorescence activation of three HBC derivatives (HBC530, HBC599 and HBC620) by different wFAPs. Solutions containing the HBC dyes, with or without wFAPs, were illuminated with 365 nm light. **f**, Fluorescence titration curves of wFAP1.1 for the HBC530, HBC599 and HBC620 fluorophores. wFAP1.1 was titrated into 50 nM HBC chromophore solutions. Both the relative fluorescence intensity and the fitted K_d are shown. Data from three experiments are presented as mean ± s.d. wFAP1.1 was highly active for HBC599 and HBC620, but very weak for HBC530. RFU, relative fluorescence unit. All structural images were generated by using PyMOL[50].

Extended Data Fig. 1). These dyes, similar to other fluorogenic dyes[9], are non-fluorescent in solution; however, they become fluorescent following binding to a specific RNA aptamer referred to as Pepper[29,30], which constrains them in a planar conformation.

We designed four-helix bundle backbones by using parametric generating equations[31–33], and utilized rotamer interaction field (RIF) docking[9] to search for favourable side-chain–ligand interactions, and to position HBC599 or HBC530 in the centre of the helical bundle scaffolds

(Fig. 1b and Extended Data Fig. 1). We used Rosetta for iterative flexible backbone design and relaxation, optimizing towards better protein–ligand interaction energy, shape complementarity to the ligand and total energy score. Folding of the designed sequences was evaluated by trRosetta[34] (for designs made before the release of AlphaFold2 (AF2)[18]) and AF2 (for a few designs made following the initial release of AF2) to filter out those that substantially deviated from the design models. Twenty sequences were selected on the basis of ranking of their energy-based scores (Methods). Genes encoding selected wFAP designs were synthesized and subsequently expressed in *Escherichia coli*. Out of the 20 wFAP designs, 16 were expressed and purified to homogeneity through nickel-affinity chromatography and size-exclusion chromatography. We assayed the designed proteins by comparing their fluorescence activation to that from the buffer. Although one design demonstrated fluorescence activation for HBC599 by about eightfold in vitro, we found it too weak for applications in more complicated environments, such as in membranes or in living cells (Extended Data Fig. 2a).

The weak activity of our initial designs may be attributed to the designed pocket structures not corresponding to their actual configurations. To design a highly stable and accurately pre-organized ligand-binding pocket for HBC599, we incorporated AF2 not merely as a final validation tool but into the phases of our design process (Fig. 1b and Extended Data Fig. 1). From the initial designs, we re-evaluated the cavity in the top 200 models using AF2 and chose 27 models with a pocket Cα root-mean-square deviation (r.m.s.d.) of less than 0.8 Å to the AF2 model for iterative optimization. This represented a much more stringent requirement for pocket pre-organization, as only 1 of the 20 early designs for experimental testing was present in these 27 models. Additionally, we resampled RIF residues to design negatively charged residues interacting with the hydroxyl group of HBC599 (Methods). The protein backbone coordinates in these models were updated by using the ones predicted by AF2. Following this, Rosetta sequence design was performed for the updated backbone, to rectify any steric clashes, to optimize side-chain packing and, when feasible, to establish new polar interactions with the ligand. Backbone coordinates were constrained to remain close to those of the AF2 models during sequence design. This iterative refinement procedure was continued until we obtained confident AF2 models containing a pocket capable of forming favourable interactions towards HBC599 (Fig. 1b).

The revised protocol effectively selected and produced designs with pockets and overall structures that closely matched the AF2 predictions—the Cα r.m.s.d. values of pocket residues were less than 0.8 Å (Extended Data Fig. 1b,c). Five genes encoding the selected designs were expressed in *E. coli*; three activated the fluorescence of HBC599 (Extended Data Fig. 2b). Among them, one design demonstrated very strong fluorescence activation, and is referred to as wFAP0 (Fig. 1c–e). We used AutoDock Vina[35] to dock HBC599 to the wFAP0 design model to assess its pocket. The binding mode in the top output from Vina docking closely matched that in the design model of wFAP0, indicating that the pocket organization was suitable for effective binding of HBC599 (Extended Data Fig. 1d).

wFAP0 was purified to homogeneity and was monomeric in solution (Extended Data Fig. 2d). Following binding, wFAP0 activated the fluorescence of HBC599 more than 280-fold in vitro, with its excitation and emission peak at 495 nm and 570 nm, respectively (Fig. 1c and Supplementary Table 1). Its absorption peak showed a notable redshift compared to that of free HBC599, indicating a marked change of the surrounding environment of the ligand due to energetically favourable interactions with wFAP0 (Extended Data Fig. 2c). wFAP0 was found to bind HBC599 with a dissociation constant (K_d) of 0.40 μM (Fig. 1d and Supplementary Table 1), which was comparable to that of other de novo-designed helical ligand-binding proteins with micromolar affinities[10,36].

To further improve the fluorescence activation of wFAP0, we performed directed evolution based on wFAP0 and identified two variants, wFAP1.1 and wFAP1.2 (Extended Data Figs. 3 and 4). The mutants showed improved brightness and binding affinity, probably through optimization of electrostatic properties around the HBC tertiary amine, as well as side-chain packing in the upper part of the protein core. wFAP1.1 and wFAP1.2 bound to HBC599 with K_d values of 58 nM and 51 nM and quantum yields of 0.88 and 0.7, respectively (Fig. 1c,d and Supplementary Table 1). The brightness of wFAP1.1 in complex with HBC599 is higher than that of the widely used enhanced green fluorescent protein[37] (Supplementary Table 1). Apo wFAP1.1 showed an all-helical circular dichroism spectrum, with thermal stability up to 95 °C (Extended Data Fig. 2f). A temperature-induced dissociation experiment indicated that the protein–ligand interaction was highly stable (Extended Data Fig. 2e). wFAP1.1 differed from wFAP1.2 in two residues in the ligand-binding pocket, and exhibited a redshift of 20 nm in its fluorescence emission maximum (Fig. 1c, Extended Data Figs. 3 and 4 and Supplementary Table 1). To investigate the influence of ligand-binding residues on the fluorescence spectrum, we created wFAP1.3 through redesigning the pocket residues in wFAP0.1. We reconfigured the charged residues that interacted with HBC599 to polar residues, and subsequently optimized the neighbouring residues (Methods). Notably, wFAP1.3 exhibited a blueshift of 30 nm in its fluorescence spectra, along with a fourfold reduction in its binding affinity to HBC599 as compared to wFAP1.1 (Fig. 1c and Supplementary Table 1).

Design of tmFAP

In the second step of our design protocol, we aimed to convert wFAPs into transmembrane proteins by redesigning the surface residues facing the membrane, while minimizing perturbance to the ligand-binding pocket structure (Fig. 2a). Initially, we tested 11 constructs designed by using the previous Rosetta protocol[2]. None of these designs showed substantial fluorescence activation compared to background signals. We attributed the failure of the initial attempt to the alteration of inter-helical packing and the destabilization of the pre-organized pocket after surface redesign, which was evident in the suboptimal recapitulation of the pocket structure by AF2 prediction.

To address these challenges, we used the ColabDesign framework[20,38] to generate sequences that accurately encode desired transmembrane protein structures (Fig. 2b and Extended Data Fig. 5a). ColabDesign allows the running of hallucination based on protein structure prediction networks such as AF2, and performs a gradient-guided search for efficient sequence update, while exposing various parts of the network for users to implement custom design functions. We utilized the backbone coordinates of the wFAP0 design as the input scaffold, and retained the protein core residues identical to those from wFAP1.1 or wFAP1.2. For each design trajectory, we hallucinated the sequence of the membrane-facing residues using the AF2 network. In addition to the default loss, we introduced two additional terms: one to promote AF2 prediction confidence and another to minimize changes in the pocket residues (Methods). We iteratively updated the transmembrane protein sequences until they accurately and confidently encoded the ligand-binding pocket. Sequence update was biased towards specific amino acid types, to generate the appropriate transmembrane span length, and adhered to the positive-inside rule for membrane localization. Besides wFAPs, we extended our pipeline to several water-soluble proteins with diverse topologies and oligomerization states. We designed a hydrophobic transmembrane span for these proteins, while specifying their core residues as a motif region and kept them fixed. The designer transmembrane proteins accurately scaffolded the target motif from the input structure, as validated by RoseTTAFold2 structure prediction (Extended Data Fig. 5a).

Six tmFAP designs were chosen for experimental evaluation from converged hallucination trajectories (Extended Data Fig. 5b–f), which exhibited more balanced amino acid composition compared to the sequences designed by the previous Rosetta protocol (Methods and

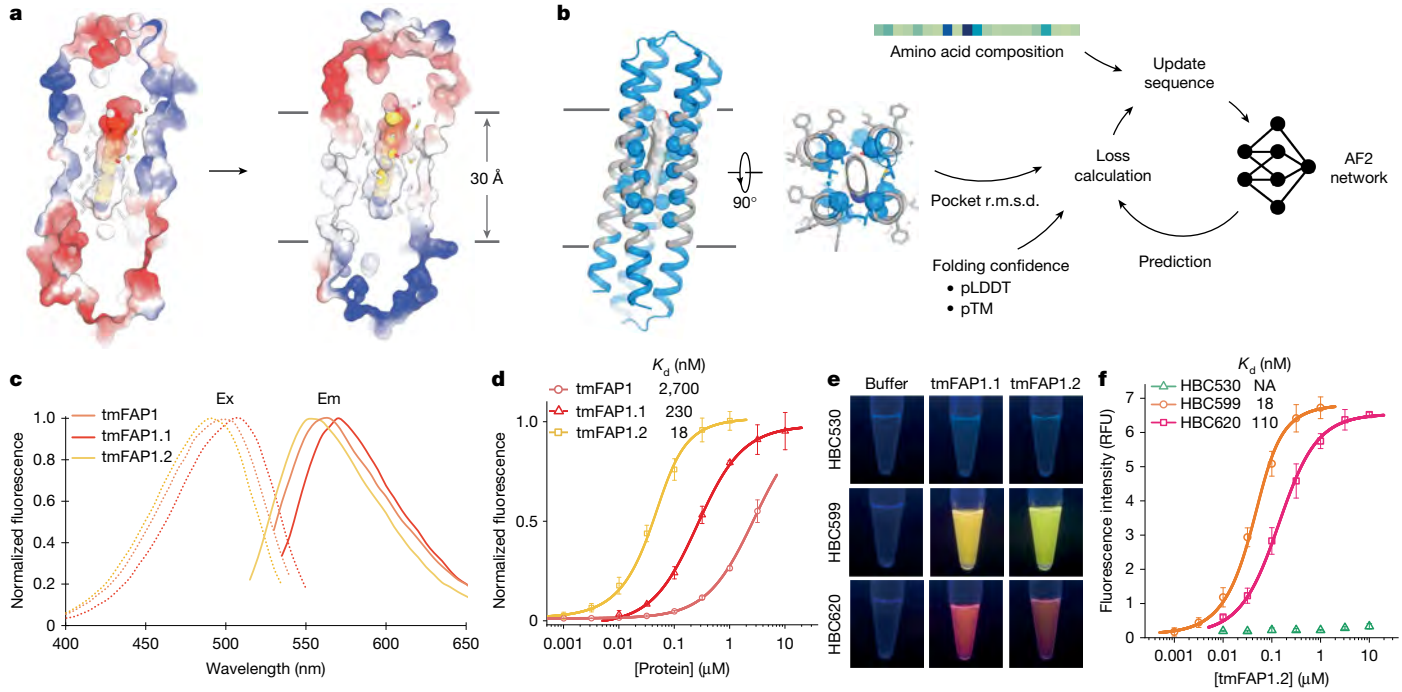

Fig. 2 | Design and characterization of tmFAPs. a, Scheme of the conversion from wFAPs (left) to tmFAPs (right) with minimal changes in the ligand-binding pocket. The electrostatic surfaces of a wFAP and a tmFAP are shown, with the latter containing a hydrophobic transmembrane span of approximately 30 Å. **b**, Design of tmFAP transmembrane span by hallucination. Left: design constraints applied to different regions of the model. wFAP0 (left) design model was used as input. Sequence of only the membrane-facing residues (grey) was redesigned. The ligand-binding pocket (shown in blue with Cα spheres) was constrained to the input coordinates. The remaining residues (shown in blue without Cα spheres) was kept fixed at the sequence level with no coordinate constraints. Right: information flow during hallucination. In each iteration, the current sequence was input to the AF2 network for inference. The output structure and metrics were then used for loss calculation. Sequence update was guided by loss and additional design restrictions. pTM, predicted template modelling score. **c**, Excitation and emission spectra of the tmFAP variants complexed with HBC599. **d**, Fluorescence titration curves of purified tmFAPs. tmFAPs at various concentrations were mixed with 50 nM HBC599. Relative fluorescence intensity was measured for each condition and used for K_d fitting. Data from three experiments are presented as mean ± s.d. **e**, Activation of the fluorescence of HBC dyes (HBC530, HBC599 and HBC620) by tmFAP1.1 and tmFAP1.2. Detergent solutions containing HBC dyes, with or without tmFAPs, were illuminated with 365 nm light. **f**, tmFAP1.2 at various concentrations was mixed with 50 nM HBC530, HBC599 or HBC620. Relative fluorescence intensity was measured for each condition and used for K_d fitting (Methods). Data from three experiments are presented as mean ± s.d. tmFAP1.2 was highly active for HBC599 and HBC620, but inactive for HBC530. NA, not applicable. All tmFAPs were solubilized in TBS buffer (pH 7.4) with 1.1% *n*-octyl-β-d-glucopyranoside.

Extended Data Fig. 5d). The pocket structures in the hallucinated designs exhibited a high level of agreement with the input model, as opposed to those designed using Rosetta (Extended Data Fig. 5e,f). Four of the six designs activated HBC599 fluorescence following expression in *E. coli*, and two designs—tmFAP1 and tmFAP2—were successfully purified to homogeneity and confirmed to be highly active in a detergent solution (Extended Data Figs. 4b,c and 6a–d). tmFAP1 was based on wFAP1.2 with one aspartic acid (H26, D51) in the pocket, whereas tmFAP2 was based on wFAP1.1 with two aspartic acids (D26, D51). Although tmFAP2 was more active, we selected tmFAP1 for further characterization and engineering on the basis of its superior expression level in *E. coli* cells. tmFAP1 bound HBC599 with a lower K_d limit of 2.7 μM and a quantum yield of 0.66 (Fig. 2c,d and Supplementary Table 1). We reasoned that although the surface sequence of tmFAP1 was favourable for *E. coli* expression, the electrostatic configuration of its core residues may not be ideal for fluorescence activation in the membrane environment. We therefore designed its core sequence to match that of tmFAP2 (wFAP1.1; Extended Data Fig. 4). This resulted in tmFAP1.1, which showed an improved K_d of 230 nM for HBC599. The sequence identity between wFAP1.1 and tmFAP1.1 is 60.2%, and they carry the same set of pocket residues. The fluorescence spectra of tmFAP1.1 was almost identical to that of wFAP1.1 (Fig. 2c–e and Supplementary Table 1).

To further improve the fluorescence activation, we carried out directed evolution, and successfully identified tmFAP1.2 and tmFAP1.3, which could be purified to homogeneity (Extended Data Figs. 3c,d and 6e–g). tmFAP1.2 showed the highest binding affinity among all of our designer FAPs, with a K_d of 18 nM and a quantum yield of 0.84 for HBC599. This affinity to HBC599 was similar to that achieved by Pepper (18 nM (ref. 29)). Additionally, a notable blueshift of about 20 nm was observed in the fluorescence spectra of tmFAP1.2 compared to tmFAP1.1, probably due to the polar mutations introduced into the protein core near the terminal cyano group of HBC599 (Fig. 2c–e, Extended Data Fig. 3c,d and Supplementary Table 1).

Notably, unlike Pepper, which activates a series of HBC derivatives with high affinity[29], the designer wFAPs and tmFAPs are highly specific to the target ligand (Figs. 1e,f and 2e,f and Extended Data Figs. 1e, 2g and 6j). We found that activation of the structurally different fluorophores HBC497, HBC508 and HBC530 by the FAP variants was weak and close to the level of nonspecific interactions, suggesting the ligands were not well stabilized to a single defined planar mode. By contrast, all FAPs except for wFAP1.3 exhibited robust activation of HBC620, a ligand containing a subtle variation of only two atoms in the condensed aromatic rings compared to HBC599. The different ligand specificity of FAPs and Pepper can be attributed to their ligand-binding modes. FAPs were designed to interact with almost all atoms of the HBC ligands, by fully encapsulating the ligands in the protein core, whereas Pepper binds to HBCs primarily through base stacking between aromatic rings, making them insensitive to modifications of the rest of the ligand structure. The ability of FAPs to selectively

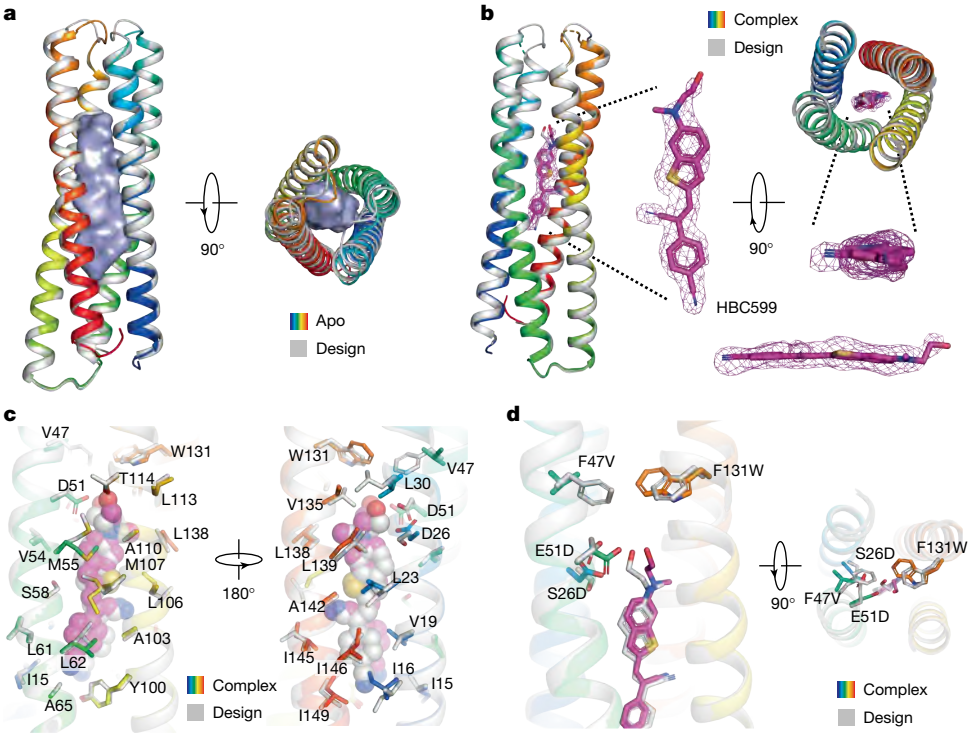

Fig. 3 | Crystal structures of both the apo form and the ligand-bound form of wFAP1.1 agree with the design models. a, Superposition of the apo structure of wFAP1.1 and the design model of wFAP0 (grey). The crystal structure is coloured blue to red from the amino to carboxy terminus. Surface of the cavity in the crystal structure is shown in light blue. **b**, Superposition of the crystal structure of wFAP1.1 in the ligand-bound form (protein chain coloured in a rainbow gradient, ligand in magenta) and the design model of wFAP0 (grey). The $F_o - F_c$ omit electron density for the ligand is contoured at 2.0σ, with F_o and F_c denoting the observed and calculated values, respectively. **c**, A close-up view of the ligand-binding site. The ligand is shown as spheres. The amino acids involved in ligand interaction are shown as sticks. **d**, A close-up view focusing on the residues that differ between wFAP0 (design) and wFAP1.1.

activate fluorophores with specific structure presents the prospect of designing a palette of orthogonal protein–dye pairs that cover a wide spectral range.

Structural validation

We conducted crystal screens for wFAPs and successfully crystallized wFAP1.1 in its apo form. We determined the structure at 2.3 Å resolution using molecular replacement with the design model (Fig. 3a, Extended Data Table 1 and Extended Data Fig. 7a,b). The structure shows a pre-organized ligand-binding pocket and closely matches the design model. The Cα r.m.s.d. values for all aligned residues and pocket-forming residues are 0.6 and 0.4 Å, respectively (Fig. 3a and Extended Data Fig. 7c–e).

We also determined the structure of wFAP1.1 in complex with HBC599 at 2.1 Å resolution, with crystals grown under the same conditions as the apo form (Extended Data Table 1 and Extended Data Fig. 7f,g). The complex structure closely resembles the design model, with an overall Cα r.m.s.d. of 0.5 Å (Fig. 3b,c and Extended Data Fig. 7h). The HBC599 chromophore in its planar conformation is nestled in the designed pocket of wFAP1.1, confirmed by unambiguous electron density in the omit map (Fig. 3b). The interface between the ligand and protein exhibits a high level of shape complementarity (0.74). The ligand-binding mode is highly consistent between the X-ray structure and the computational model—the r.m.s.d. values for the 29 Cα atoms of residues involved in ligand interaction and for all heavy atoms of the ligand are 0.4 Å and 1.27 Å, respectively (Fig. 3c,d). We used AutoDock Vina to dock HBC599 to the wFAP1.1 crystal structure, and found that the ligand structure in the top output closely matched the crystal structure (Extended Data Fig. 9a). Docking HBC620 to the structure yielded a model very close to that with HBC599, showing that the pocket can accommodate HBC620 in a very similar binding mode (Extended Data Fig. 9b).

In comparison to the original design wFAP0, wFAP1.1 carried four alterations because of evolution (Fig. 3d). Two alterations—F47V and F131W—did not form direct interactions with the ligand, but probably optimized the core packing of the protein. Similar to the Glu51 in the wFAP0 design model, Asp51 in wFAP1.1 also formed a hydrogen bond with the terminal hydroxyl group of HBC599. The S26D alteration introduced an additional negatively charged residue close to the tertiary amine in HBC599, which becomes positively charged following excitation. The introduction of additional negatively charged residues probably reduced the energy gap between the highest occupied molecular orbital and the lowest unoccupied molecular orbital of the fluorophore, and ultimately induced a bathochromic shift in the fluorescence spectra of wFAPs.

For structural characterization of tmFAPs, we first conducted crystal screens, both with and without HBC599, but were unable to obtain crystals. We then attempted structure determination by cryogenic electron microscopy (cryo-EM) despite the small size of tmFAPs. We grafted the apocytochrome b562 protein BRIL[39] to tmFAP1.1 through two de novo-designed rigid helical linkers, replacing the intracellular loop between TM2 and TM3, while keeping the sequence of the BRIL domain and the rest of tmFAP1.1 fixed. We selected four sequences for experimental testing, and all showed strong fluorescence activation for HBC599. The most active fusion construct was tmFAP1.1–BRIL, which activated the fluorescence of HBC599 with a K_d of 167 nM (Extended Data Fig. 6i).

We determined the cryo-EM structure of tmFAP1.1–BRIL in complex with HBC599 and an anti-BRIL antigen-binding fragment (Fab) at a resolution of 2.79 Å (Fig. 4, Extended Data Table 2 and Extended Data Fig. 8). The cryo-EM map revealed four transmembrane helices, the

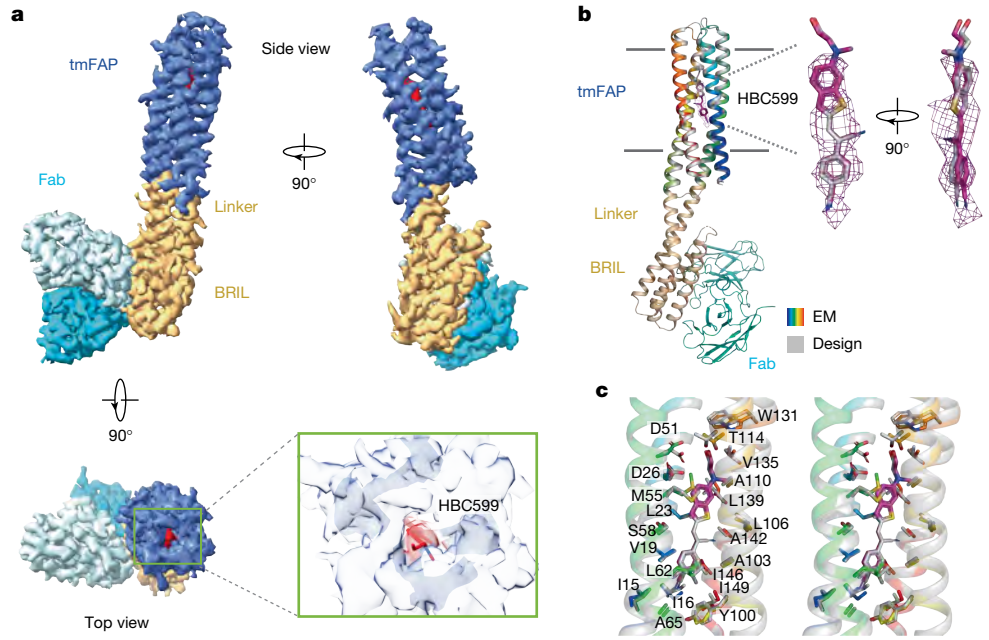

Fig. 4 | Cryo-EM structure of tmFAP1.1–BRIL complexed with HBC599. **a**, Three different views of the cryo-EM density map of tmFAP1.1–BRIL bound to an anti-BRIL Fab. The HBC599 density is depicted in red. **b**, Superposition of the cryo-EM structure of the tmFAP1.1–BRIL–HBC599 complex and the tmFAP1.1 design model (grey). The cryo-EM structure is coloured in a rainbow gradient with the ligand in magenta. The EM density of the ligand is contoured at 3.0σ. **c**, A stereo view (cross-eye) of the ligand-binding site in the tmFAP1.1 EM structure (rainbow) superposed with the design model (grey). The ligand in the EM structure is shown in magenta. The amino acids surrounding the ligand are depicted as sticks.

BRIL domain and the variable region of the anti-BRIL Fab, as well as the designed linker connecting the transmembrane domain and the BRIL domain (Fig. 4a and Extended Data Fig. 8). The density surrounding the membrane-spanning region probably originates from surrounding detergent molecules (Extended Data Fig. 8f). Notably, the cryo-EM structure of the transmembrane domain of tmFAP1.1–BRIL closely resembled the design model of tmFAP1.1, with a Cα r.m.s.d. of 0.74 Å for all aligned residues (Fig. 4b,c). The density of the ligand HBC599 was well resolved, and the fluorophore exhibited a structure nearly identical to that in the computational model. Residues involved in ligand interaction also assume similar positions in both the cryo-EM structure and the design model (Fig. 4b,c).

The HBC599 molecule is entirely enclosed within the core of the designer four-helix bundle (Fig. 4a,b). This binding mode is reminiscent of some small-molecule transporters adopting the substrate-bound occluded conformation, in which the ligands were entirely encapsulated by the proteins during the substrate transport cycle[40]. The protein must undergo a conformational change or protein breathing motions—possibly driven by thermodynamics—to allow ligand access.

To validate the protein–ligand interactions in designer FAPs, we examined the impact of single amino-acid substitutions within the ligand-binding pocket of tmFAP1.1 and wFAP1.1. Substitution of small nonpolar residues with large aromatic residues mostly resulted in the complete abolishment of fluorescence activation (V19Y, S58F, A103Y and A142Y), whereas the L23Y substitution led to a substantial reduction (Extended Data Fig. 9c,d). Similarly, alterations of key residues to alanine (D26A, D51A, Y100A, M107A and W131A) abolished or reduced the level of fluorescence activation in both proteins. The mutagenesis data, together with the spectral data, are consistent with our structures, showing that tmFAP1.1 binds HBC599 in a mode very similar to that of wFAP1.1, and that the pocket residues are critical for fluorescence activation. Additionally, for the two proteins wFAP1.1 and tmFAP1.1, we observed a strong negative correlation between the predicted local distance difference test (pLDDT) values in the predicted structures and the B-factors in the experimentally determined structures (Extended Data Fig. 9e,f). This suggests that pLDDT values may serve as a useful indicator of structural stability and motion, thereby facilitating the assessment of de novo designed proteins.

Fluorescence activation in live cells

Both wFAPs and tmFAPs exhibited specific and strong fluorescence activation for HBC599 in live *E. coli* and Chinese hamster ovary (CHO) cells (Fig. 5a,b). Following the addition of HBC599, cells expressing FAPs demonstrated strong fluorescence activation, whereas those not expressing FAPs exhibited minimal background fluorescence activation (Fig. 5a,b). In the case of cytosolic expression, wFAP1.1 exhibited clear fluorescence across the entire cellular region in both *E. coli* and CHO cells. Moreover, when fused with the mitochondrial outer membrane protein synaptojanin 2 binding protein (SYNJ2BP), wFAP1.1 exhibited fluorescence localized to the mitochondria of CHO cells. By contrast, *E. coli* cells expressing tmFAP1.2 exhibited robust fluorescence in the membrane enveloping the fluorescently ineffective cytoplasm. CHO cells expressing tmFAP1.1 exhibited strong fluorescence within intracellular endomembrane systems (Extended Data Fig. 6l).

To develop a tmFAP compatible with the plasma membrane of eukaryotic cells, we fine-tuned surface residues of tmFAP1.1. We revised our transmembrane hallucination protocol, in which the transmembrane length was increased as eukaryotic cell membranes are generally thicker than those of bacteria. We also emphasized the positive-inside rule, by designing more positively charged residues in the RK ring, and replaced the WY ring by a negatively charged DE ring. A redesigned variant tmFAP3 localized to the plasma membrane in *Xenopus* oocytes and activated bright fluorescence of HBC599 (Fig. 5c and Extended Data Figs. 4 and 6h,k,m). In CHO cells, tmFAP3 strongly activated the fluorescence of HBC599; however, tmFAP3 localized to both the plasma membrane and endomembrane systems (Fig. 5b and Extended Data Fig. 6k). This is probably due to the

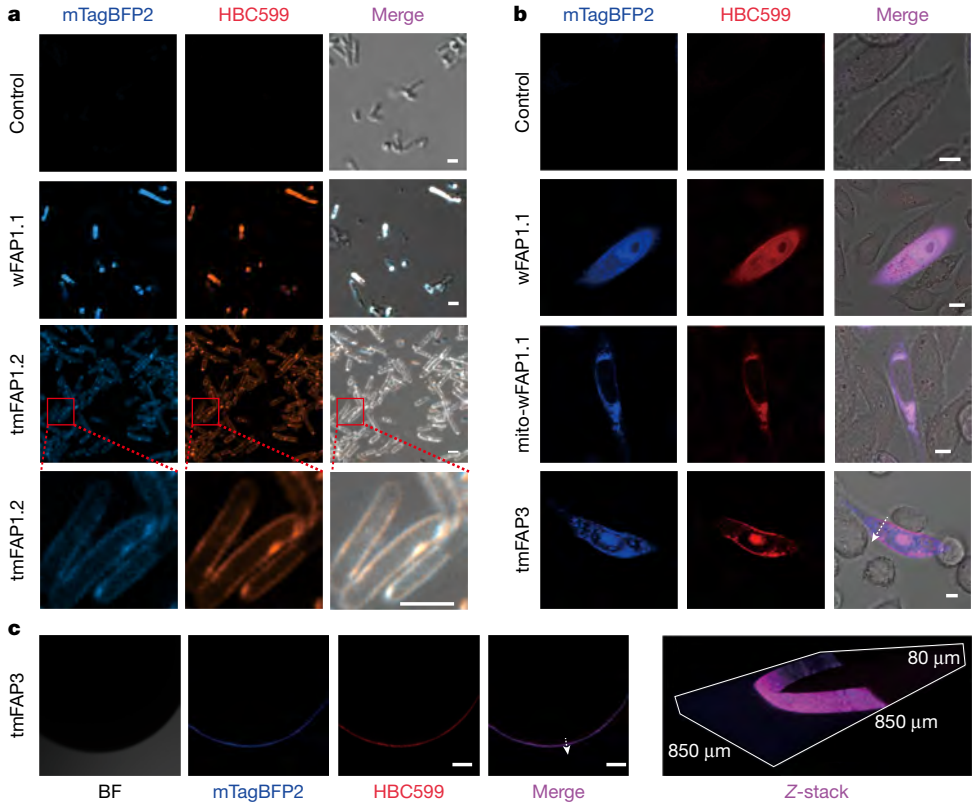

Fig. 5 | Fluorescence activation in live cells. Live-cell imaging of fluorescence activation by wFAPs and tmFAPs. **a**,**b**, Live *E. coli* (**a**) and CHO (**b**) cells were imaged in the presence of 200 nM (**a**) and 20 nM (**b**) HBC599. The designer wFAPs and tmFAPs were genetically fused with mTagBFP2 (a blue fluorescent protein variant) at the C terminus to indicate their localization. Fluorescence signals of mTagBFP2 (blue, left columns) and HBC599 (red, middle columns) were recorded and overlaid with the corresponding brightfield images (right columns). Uninduced *E. coli* cells (**a**, top row) and untransfected CHO cells (**b**, top row) showed minimal background signal when imaged under the same conditions and HBC599 concentration as those expressing FAPs. wFAP1.1 was bright and homogeneous in the cytosol of both *E. coli* (**a**, row 2) and CHO (**b**, row 2) cells, whereas it was localized to mitochondria when fused with the mitochondrion-targeting signal SYNJ2BP (**b**, row 3). tmFAP1.2 (**a**, rows 3 and 4) and tmFAP3 (**b**, row 4) clearly localized to the cell membrane of *E. coli* (**a**) and the membrane fraction of CHO cells (**b**) with bright HBC599 fluorescence. **c**, tmFAP3 localized to the plasma membrane and showed bright fluorescence activation of HBC599 in *Xenopus* oocytes. Fluorescence signals of mTagBFP2 (image 2) and HBC599 (image 3) were recorded in the presence of 20 nM HBC599 and overlaid (image 4). The corresponding brightfield (BF) image is shown in image 1. Image 5 (*Z*-stack) shows a patch of oocyte cell membrane reconstructed from a series of focal planes. Line scans of the mTagBFP2 and HBC599 channels (in **b**,**c**; dashed white arrows) across the membranes are shown in Extended Data Fig. 6. Scale bars, 2 µm (**a**), 10 µm (**b**) and 100 µm (**c**). At least two independent experiments were conducted, yielding consistent outcomes.

intricate membrane protein trafficking and folding mechanisms in mammalian cells. tmFAPs could be developed as a tool for investigating membrane protein biogenesis, in which the correct folding of tmFAPs in different membrane systems can be indicated by the fluorescence signal.

Conclusions

This work presents the accurate de novo design of ligand-binding transmembrane proteins. The high-resolution cryo-EM structure of the tmFAP–HBC599 complex showed that the interactions between artificial chemicals and transmembrane proteins within the membrane can be accurately designed. We compared tmFAPs to rhodopsins, the natural fluorescent membrane proteins that have been developed for various membrane-sensing purposes (Fig. 6). tmFAP1.2 is almost 1,000 times brighter than archaerhodopsin-3 (refs. 41,42), a rhodopsin under extensive engineering for voltage sensing[43–45]. The brightness and quantum yield of tmFAP1.2 exceed those of NeoR[46], the brightest rhodopsin reported. Moreover, whereas all rhodopsins are limited to the seven-helix topology and the covalently attached retinal as their fluorophore, tmFAP contains only four transmembrane helices and non-covalently binds to an artificial chemical ligand, HBC599. Our advance goes beyond engineering and repurposing naturally occurring ligand-binding transmembrane proteins, which is restricted to native protein scaffolds and a limited choice of ligands.

The successful design of bright wFAPs and tmFAPs exemplifies the robust nature of our two-step approach for designing ligand-binding transmembrane proteins. The utilization of deep neural networks has facilitated the design of both the ligand-accommodating scaffolds and the transmembrane span. Regarding scaffold generation, the incorporation of AF2 has substantially improved the sampling efficiency and designability of the scaffolds. For the transmembrane span design, deep network hallucination effectively minimized alternative associations among the hydrophobic transmembrane domains, and generated protein sequences that correctly fold with a predefined pocket structure. Notably, the deep network was trained using structures from the Protein Data Bank, which contains a substantially lower number of membrane protein structures compared to soluble protein structures. Despite this scarcity of membrane protein structures, it has been reported that AF2 predicts both transmembrane proteins and soluble proteins with comparable accuracy[47]. We show that, from a design perspective, the deep network enables the design of functional transmembrane proteins and achieves a high level of efficiency and accuracy.

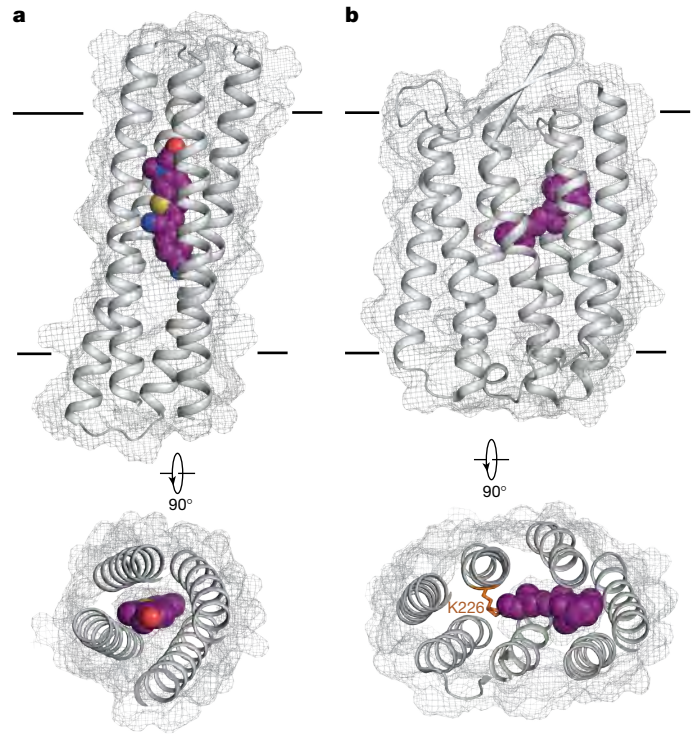

Fig. 6 | Comparison of structures and ligand-binding modes of tmFAP and archaerhodopsin-3. a,**b**, Surface mesh and cartoon representation of structure models of the de novo-designed tmFAP (**a**) and the natural fluorescent transmembrane protein archaerhodopsin-3 (**b**, Protein Data Bank ID: 6S6C (ref. 51)). Chromophores are visualized as spheres. Chromophores of both proteins are completely enclosed within the protein core. The retinal chromophore in archaerhodopsin-3 is oriented almost parallel to the membrane, and is covalently linked to the protein through Lys226 (orange sticks). The HBC599 chromophore in tmFAP lies nearly perpendicular to the membrane, and is non-covalently bound to the protein. Archaerhodopsin-3 consists of seven transmembrane helices, whereas tmFAP possesses only four.

Our design approach enables the exploration of a variety of de novo helical bundle scaffolds and allows the incorporation of different fluorophores with desired properties for fluorescence-based imaging applications. The embedding of the fluorophore within the membrane may allow direct sensing of the chemical gradient or physical properties across the membrane, such as the pH gradient and membrane potential[48]. Our de novo approach offers a unique method for creating hybrid indicators[44,45] in membranes, which directly incorporate synthetic dyes into genetically encoded transmembrane proteins, combining the advantages of both small molecules (high sensitivity) and proteins (specific localization). The non-covalent binding of chromophores by tmFAPs may allow photobleached dyes to be replaced by fresh dyes in solution during long-term imaging, enabling continuous fluorescence emission[49]. Our work serves as a step towards the de novo design of a new generation of transmembrane proteins that accommodate functional ligand sites within the membrane, such as sensors, receptors, transporters, ion channels and enzymes.

Online content

Any methods, additional references, Nature Portfolio reporting summaries, source data, extended data, supplementary information, acknowledgements, peer review information; details of author contributions and competing interests; and statements of data and code availability are available at https://doi.org/10.1038/s41586-025-08598-8.

1. Joh, N. H. et al. De novo design of a transmembrane Zn^{2+}-transporting four-helix bundle. *Science* **346**, 1520–1524 (2014).
2. Lu, P. et al. Accurate computational design of multipass transmembrane proteins. *Science* **359**, 1042–1046 (2018).
3. Xu, C. et al. Computational design of transmembrane pores. *Nature* **585**, 129–134 (2020).
4. Scott, A. J. et al. Constructing ion channels from water-soluble alpha-helical barrels. *Nat. Chem.* **13**, 643–650 (2021).
5. Vorobieva, A. A. et al. De novo design of transmembrane β barrels. *Science* **371**, eabc8182 (2021).
6. Berhanu, S. et al. Sculpting conducting nanopore size and shape through de novo protein design. *Science* **385**, 282–288 (2024).
7. Tinberg, C. E. et al. Computational design of ligand-binding proteins with high affinity and selectivity. *Nature* **501**, 212–216 (2013).
8. Polizzi, N. F. et al. De novo design of a hyperstable non-natural protein–ligand complex with sub-Å accuracy. *Nat. Chem.* **9**, 1157–1164 (2017).
9. Dou, J. et al. De novo design of a fluorescence-activating beta-barrel. *Nature* **561**, 485–491 (2018).
10. Polizzi, N. F. & DeGrado, W. F. A defined structural unit enables de novo design of small-molecule binding proteins. *Science* **369**, 1227–1233 (2020).
11. Lu, L. et al. De novo design of drug-binding proteins with predictable binding energy and specificity. *Science* **384**, 106–112 (2024).
12. An, L. et al. Binding and sensing diverse small molecules using shape-complementary pseudocycles. *Science* **385**, 276–282 (2024).
13. Zhu, J. & Lu, P. Computational design of transmembrane proteins. *Curr. Opin. Struct. Biol.* **74**, 102381 (2022).
14. Cordova, J. M., Noack, P. L., Hilcove, S. A., Lear, J. D. & Ghirlanda, G. Design of a functional membrane protein by engineering a heme-binding site in glycophorin A. *J. Am. Chem. Soc.* **129**, 512–518 (2007).
15. Korendovych, I. V. et al. De novo design and molecular assembly of a transmembrane diporphyrin-binding protein complex. *J. Am. Chem. Soc.* **132**, 15516–15518 (2010).
16. Hardy, B. J. et al. Cellular production of a de novo membrane cytochrome. *Proc. Natl Acad. Sci. USA* **120**, e2300137120 (2023).
17. Senior, A. W. et al. Improved protein structure prediction using potentials from deep learning. *Nature* **577**, 706–710 (2020).
18. Jumper, J. et al. Highly accurate protein structure prediction with AlphaFold. *Nature* **596**, 583–589 (2021).
19. Baek, M. et al. Accurate prediction of protein structures and interactions using a three-track neural network. *Science* **373**, 871–876 (2021).
20. Wang, J. et al. Scaffolding protein functional sites using deep learning. *Science* **377**, 387–394 (2022).
21. Anishchenko, I. et al. De novo protein design by deep network hallucination. *Nature* **600**, 547–552 (2021).
22. Dauparas, J. et al. Robust deep learning–based protein sequence design using ProteinMPNN. *Science* **378**, 49–56 (2022).
23. Watson, J. L. et al. De novo design of protein structure and function with RFdiffusion. *Nature* **620**, 1089–1100 (2023).
24. Wicky, B. I. M. et al. Hallucinating symmetric protein assemblies. *Science* **378**, 56–61 (2022).
25. An, L. et al. Hallucination of closed repeat proteins containing central pockets. *Nat. Struct. Mol. Biol.* **30**, 1755–1760 (2023).
26. Yeh, A. H.-W. et al. De novo design of luciferases using deep learning. *Nature* **614**, 774–780 (2023).
27. Krishna, R. et al. Generalized biomolecular modeling and design with RoseTTAFold All-Atom. *Science* **384**, eadl2528 (2024).
28. Fairman, J. W., Noinaj, N. & Buchanan, S. K. The structural biology of β-barrel membrane proteins: a summary of recent reports. *Curr. Opin. Struct. Biol.* **21**, 523–531 (2011).
29. Chen, X. et al. Visualizing RNA dynamics in live cells with bright and stable fluorescent RNAs. *Nat. Biotechnol.* **37**, 1287–1293 (2019).
30. Huang, K. et al. Structure-based investigation of fluorogenic Pepper aptamer. *Nat. Chem. Biol.* **17**, 1289–1295 (2021).
31. Grigoryan, G. & DeGrado, W. F. Probing designability via a generalized model of helical bundle geometry. *J. Mol. Biol.* **405**, 1079–1100 (2011).
32. Thomson, A. R. et al. Computational design of water-soluble alpha-helical barrels. *Science* **346**, 485–488 (2014).
33. Huang, P. S. et al. High thermodynamic stability of parametrically designed helical bundles. *Science* **346**, 481–485 (2014).
34. Yang, J. et al. Improved protein structure prediction using predicted interresidue orientations. *Proc. Natl Acad. Sci. USA* **117**, 1496–1503 (2020).
35. Eberhardt, J., Santos-Martins, D., Tillack, A. F. & Forli, S. AutoDock Vina 1.2.0: new docking methods, expanded force field, and Python bindings. *J. Chem. Inf. Model.* **61**, 3891–3898 (2021).
36. Thomas, F. et al. De novo-designed α-helical barrels as receptors for small molecules. *ACS Synth. Biol.* **7**, 1808–1816 (2018).
37. Sarkisyan, K. S. et al. Green fluorescent protein with anionic tryptophan-based chromophore and long fluorescence lifetime. *Biophys. J.* **109**, 380–389 (2015).
38. Frank, C. et al. Scalable protein design using optimization in a relaxed sequence space. *Science* **386**, 439–445 (2024).
39. Emsley, P. & Cowtan, K. Coot: model-building tools for molecular graphics. *Acta Crystallogr. D* **60**, 2126–2132 (2004).
40. Yan, N. Structural biology of the major facilitator superfamily transporters. *Annu. Rev. Biophys.* **44**, 257–283 (2015).
41. Chow, B. Y. et al. High-performance genetically targetable optical neural silencing by light-driven proton pumps. *Nature* **463**, 98–102 (2010).
42. Mclsaac, R. S. et al. Directed evolution of a far-red fluorescent rhodopsin. *Proc. Natl Acad. Sci. USA* **111**, 13034–13039 (2014).

43. Kralj, J. M., Douglass, A. D., Hochbaum, D. R., Maclaurin, D. & Cohen, A. E. Optical recording of action potentials in mammalian neurons using a microbial rhodopsin. *Nat. Methods* **9**, 90–95 (2011).
44. Abdelfattah, A. S. et al. Bright and photostable chemigenetic indicators for extended in vivo voltage imaging. *Science* **365**, 699–704 (2019).
45. Liu, S. et al. A far-red hybrid voltage indicator enabled by bioorthogonal engineering of rhodopsin on live neurons. *Nat. Chem.* **13**, 472–479 (2021).
46. Broser, M. et al. NeoR, a near-infrared absorbing rhodopsin. *Nat. Commun.* **11**, 5682 (2020).
47. Hegedus, T., Geisler, M., Lukacs, G. L. & Farkas, B. Ins and outs of AlphaFold2 transmembrane protein structure predictions. *Cell. Mol. Life Sci.* **79**, 73 (2022).
48. Kralj, J. M., Hochbaum, D. R., Douglass, A. D. & Cohen, A. E. Electrical spiking in *Escherichia coli* probed with a fluorescent voltage-indicating protein. *Science* **333**, 345–348 (2011).
49. Kwon, J. et al. Bright ligand-activatable fluorescent protein for high-quality multicolor live-cell super-resolution microscopy. *Nat. Commun.* **11**, 273 (2020).
50. The PyMOL Molecular Graphics System v1.8 (Schrodinger, 2015).
51. Bada Juarez, J. F. et al. Structures of the archaerhodopsin-3 transporter reveal that disordering of internal water networks underpins receptor sensitization. *Nat. Commun.* **12**, 629 (2021).

Methods

Computational design of soluble HBC-binding proteins

Parametric scaffold generation. To generate idealized helices for RIFdock, we used the Rosetta BundleGridSampler[52] to sample the following parameters: w_0 (super helical twist), r_0 (major helix radius), $\Delta\omega_1$ (rotation about the helix's own axis) and z_0 offset (displacement along the helical bundle's z axis). Two helices were independently sampled for r_0 and $\Delta\omega_1$ values, with the remaining two helices generated through applying C_2 symmetry. Each helix consisted of 35 residues, yielding helical bundles with sufficient length for a 30-Å transmembrane span. The four helices were assembled into a bundle using ConnectChainsMover, by constructing three short rigid loops.

RIF docking. We used RIFgen to generate de novo side chains that potentially interact with the two cyano groups and the hydroxyl group of HBC599. Using Avogadro[53], coordinates were generated for HBC599 in either *cis* or *trans* planar conformations, both theoretically ideal for fluorescence. During subsequent design steps, torsion angles within the HBC π-conjugation system were held constant. The aliphatic tail was left flexible, and its conformation was generated using Open Babel[54]. Initially, 60 ligand conformations were utilized for RIF docking against parametric scaffolds, and this number was increased to 230 at the fine-tuning stage of docking against optimized scaffolds. Considering the partial positive charge of the tertiary amine during fluorescence activation, we explicitly sampled for Glu and Asp residues interacting with the hydroxyl group, to design a negatively charged pocket. As the version of RIFdock we used was not compatible with certain chemical groups in the ligands, we substituted the –CN groups with –C = O groups in HBC599 for interaction searches. After the RIFdock step, ligands were reverted to their original atom configuration, and scored by Rosetta for subsequent filtering.

We used RIFdock to place the ligand at the centre of the helical bundles. We required the output models to contain no clash between the ligand and scaffolds, and the hydroxyl group on HBC to be satisfied by hydrogen bonds. For RIF residues containing unsatisfied heavy atoms, we used HBNet to search for hydrogen-bond networks. Models were discarded if any polar heavy atoms remained unsatisfied after HBNet search.

Sequence design. The filtered RIFdock outputs underwent one round of quick fix-backbone sequence design. We score the output ligand-binding pocket by interface energy and shape complementarity, to filter for models with promising pocket configurations. Side-chain packing also serves the purpose of initializing the sequence of the helical bundles, to limit the deviation of backbone coordinates in the following flexible backbone design.

We use a flexible backbone sequence design protocol to optimize the models. The protocol performs a short simulated-annealing trajectory, with each step first designing sequence for the binding pocket, and then optimizing packing of the rest of the helical bundle. During design of the pocket residues, the identity of the rest of the residues was fixed, but rotamer repacking was allowed. For pocket sequence design, we searched for favourable ligand–protein side-chain interactions by packing ligand neighbour residues, followed by Cartesian minimization. During design of the rest of the helical bundle, we sampled sequences for stable helical bundles, with the pocket residue sequence fixed but rotamer repacking allowed. During design, RIF residues were fixed to their original rotamers, and atom distance constraints were applied to ensure any hydrogen bonds with the ligand were retained. Acceptance criteria of the simulated annealer included total score, interface energy, shape complementarity and number of buried unsatisfied atoms.

AF2 prediction. AF2 prediction was run using a local installation of ColabFold 1.3.0[55], for both scaffold generation during design and for final validation of the models. We ran AF2 in the single-sequence mode, with three recycles, followed by AMBER relaxation. The rest of the settings were default unless otherwise specified. We used the top model (ranked by pLDDT) for the scaffold update step in the design stage. We used all five AF2 models for validation of wFAPs and Rosetta-designed tmFAPs. AF2 model 5 was used for validation of hallucination-generated sequences.

Iterative scaffold and sequence optimization. Although the protocol used for our early designs could produce models that were ideal according to energy-based metrics and human investigation, we found it challenging to evaluate whether the output sequences will actually fold into a structure with the target pre-organized pocket, by using solely the energy-based design methods. Switching to more accurate energy functions or increasing the sampling space, for example, using Cartesian energy functions or ab initio folding, could result in more accurate models. However, such sampling would markedly increase the computation time and reduce sampling efficiency.

To address this, we incorporate the highly accurate AF2 network with the energy-based explicit ligand modelling. We start the iterative optimization by using AF2 to generate backbone coordinates for sequences from the flexible backbone design protocol. Although the AF2 network could model only protein chains, in many cases we found it was able to output structures with pre-organized pockets, indicating either that the scaffold was stable enough to support pre-organization of the pocket, or that AF2 implicitly modelled the missing atoms or chains. AF2 prediction models were aligned to the energy-based designs, and models with pocket Cα r.m.s.d. < 0.8 Å were selected for further design. In these models, the protein chains were replaced by the corresponding AF2 models. During Rosetta sequence design, backbone movement was restricted by applying coordinate constraints to Cα atoms, with a bound width of 0.1 for the pocket region and 0.5 for the other region, until the next AF2 prediction. We referred to this process as scaffold update.

We then performed 'sequence update' for these updated models. One round of sequence design was first carried out at the binding pocket, to sample for potential new polar interactions with the ligand, and to resolve any major steric clashes. Sequences were further optimized by Rosetta flexible backbone design and relax protocols with the above-mentioned backbone coordinate constraints. We experimented with altering amino acid composition, by reducing hydrophobic aliphatic residues, especially Leu and Ile, and encouraged more aromatic residues by preventing Trp, Tyr and Phe from being designed away once chosen during sampling. This resulted in better AF2 metrics in some design iteration trajectories. Outputs that passed the energy-based metrics were fed into the AF2 network again, for the next iteration of optimization. We optimized for convergence between the coordinates and the sequence encoding the ligand-binding pocket. Models with AF2 prediction pocket Cα r.m.s.d. < 0.8 Å and pLDDT > 85 were collected for experimental testing. For the design of wFAPs, we observed convergence after 1 to 3 iterations. Trajectories were discarded with no convergence after three iterations. Overall Cα r.m.s.d. and pocket Cα r.m.s.d. between wFAP0 and its original input are 1.1 Å and 0.5 Å, respectively. wFAP0 went through three iterations.

For the redesign performed to make wFAP1.3, we searched polar but non-charged interactions by RIFdock against the wFAP0 scaffold. We then performed an HBNet search to resolve any unsatisfied polar atoms. We also redesigned the neighbouring residues to optimize the packing of side chains by Rosetta and predicted the design by AF2.

Computational design of transmembrane HBC-binding proteins

There are several reasons why the design of transmembrane ligand-binding proteins is challenging. First, de novo design of water-soluble ligand-binding proteins with high affinity and specificity remains a challenge despite progress in the recent years and, in particular, it is unclear whether the design principles and methods can be extended

to transmembrane proteins. Second, specific folds and pocket configurations are required for transmembrane ligand-binding proteins. To be able to traverse the membrane, proteins typically adopt either an all-α or all-β topology, and necessitate a transmembrane span with specific length. Third, introducing cavities into transmembrane proteins generally destabilizes the proteins owing to a reduction in the density of packing and the burial of polar ligand-interacting residues within the membrane. The redesign of a large portion of the surface residues to nonpolar residues for membrane traversing further complicates protein folding, making it challenging to accurately scaffold functional sites in transmembrane proteins. In this case, the design task presented a challenge due to the necessity of mutating nearly 1/3 of the total residues (47 out of 161 in the case of wFAP0) to generate the highly hydrophobic transmembrane span. Consequently, the proportion of nonpolar residues in the protein increased to 63% (Extended Data Fig. 4), thereby raising the probability of deformation or collapse of the ligand-binding pocket. Fourth, transmembrane proteins are encircled by a substantial concentration of lipids and a strong electric field across the membrane, which can potentially alter protein–ligand interaction by inducing conformation changes in proteins or blocking ligand entrance. Fifth, the biochemical and structural characterization of membrane proteins presents greater experimental challenges in comparison to water-soluble proteins.

Sequence initialization for conversion to tmFAPs. To convert wFAPs to tmFAPs, we first used the protocol described in a previous study for designing multi-pass transmembrane proteins[2]. Briefly, we first oriented the design models for wFAPs to be perpendicular to the membrane plane. The hydrophobic transmembrane span, the WY ring and the RK ring were then configured on the basis of a 30-Å membrane. The sequences of these regions were designed by a Rosetta fix-backbone design protocol. Specifically, we constrained the fraction or number of amino acids on the transmembrane span per model as follows: only Leu, Ile, Val, Ala, Met and Phe were allowed; the Leu and Ile fraction was 0.15–0.4; the Val fraction was 0.15–0.3; the Ala fraction was 0.05–0.15; and the Met absolute number was 0 or 1. The extramembrane surface residues were fine-tuned by rational design, according to the positive-inside rule. The designed models were used as the input for partial hallucination.

The above initialization strategy was implemented in our initial attempt, and the subsequent hallucination readily generated high-quality designs. In further testing, we found hallucination output with similar quality could be generated using simpler initialization strategies, or starting directly from a water-soluble sequence. This could allow the network to explore different sequence space. The specific initialization sequence we used for tmFAPs was the sequence of a failed design generated by the traditional methods. This sequence could be folded by AF2, but its pocket deviated substantially from that of wFAP0 (pLDDT = 89, pocket Cα r.m.s.d. = 2.4 Å, calculated using the worst AF2 model). This sequence was also experimentally tested and was found inactive for HBC599.

Hallucination of the transmembrane sequences. The transmembrane sequence of tmFAPs was designed using the ColabDesign[38] framework, version 1.1.1. Code was adapted from the partial hallucination design protocol, executed with a local installation of the software. The above-described template was used as the input pdb file. Ligand-interacting residues were defined as a motif for distogram_cce and r.m.s.d. calculation. For positions outside the transmembrane region, sequence design was not allowed, whereas changes in coordinates would incur no penalty. At the designable positions, we incorporated the empirical amino acid bias for various transmembrane regions, such as the hydrophobic transmembrane span, the RK ring, the DE ring, the WY ring and extracellular regions[2], into the sequence update procedure of the gradient-guided hallucination. To encourage fast convergence, we removed most of the amino acid composition constraints in the hydrophobic transmembrane span used in the previous Rosetta protocol, emphasizing only a nonpolar surface and limiting the number of Met and Gly residues (all the polar amino acids, Pro and Cys were turned off by default).

Three recycles were used for inference, as we observed that the network failed to fold certain sequences with fewer recycles. For the design of tmFAPs, we found our loss weights setting distogram_cce = 1, r.m.s.d. = 1, pLDDT = 1, contacts = 0 gave efficient converge in the case of tmFAPs. We used the design_pssm_semigreedy protocol, with 300 steps of relaxed sequence-space design, followed by 200–300 steps of one-hot sequence optimization. Hallucination was performed using AF2 model 1–4, with model 5 held-out for validation. We also tested RoseTTAFold2[56] and ESMFold[57] predictions as additional evaluation methods for tmFAPs, of which the results are consistent with those of AF2 (Extended Data Fig. 5f). For more challenging targets, we found that increasing design steps and allowing simultaneous redesign of the loop sequences could be essential for convergence.

The design restrictions and amino acid bias were implemented by modifying the gradient during sequence update. Prohibition of updating towards a specific sequence at a specific position was achieved by adding a large negative bias to the gradient. Specifically, this allowed controlling of the sequence design region, and the amino acid identity of the hydrophobic transmembrane span. Promoting or disfavouring certain amino acid types at specific regions, such as increasing Arg and Lys in the RK ring or reducing Met and Gly in the transmembrane span, was implemented through multiplying the corresponding gradient value by a factor. The WY ring and RK ring were implemented by enabling update to WY or RK at their corresponding positions, with no additional modification of the gradient.

For tmFAPs, the output sequences were validated by structure prediction using AF2 model 5. We filtered for outputs with pLDDT > 85 and pocket Cα r.m.s.d. < 0.8 Å for experimental characterization. For other targets, sequences were hallucinated using all five AF2 models, and filtered using the same pLDDT and Cα r.m.s.d. criteria. Validation was performed using RoseTTAFold2.

Computational design of rigid fusion linkers

To design the tmFAP–BRIL fusion, we sampled linker length and generated two initial scaffolds using RFDiffusion[23], and designed the linker sequence using ProteinMPNN[22]. The sequences of the BRIL domain and tmFAP were kept fixed during design. The designed sequences were assessed by AF2, and the best AF2 models were used as the input scaffold for a new round of sequence design. After 2–3 rounds of design iterations, we were able to obtain sequences confidently encoding both the BRIL domain and the ligand-binding pocket structure in the original tmFAP1.1 model. RFDiffusion was obtained and run according to https://github.com/RosettaCommons/RFdiffusion. ProteinMPNN was obtained and run according to https://github.com/dauparas/ProteinMPNN.

Additional validation by RoseTTAFold2 and ESMFold

RoseTTAFold2 was installed and run according to https://github.com/uw-ipd/RoseTTAFold2. Predictions were run in the single-sequence mode, with 10 recycles for all sequences except for tm-GFF18 and tm-GLF32 (20 recycles). C_2 symmetry was specified for tm-C2. ESMFold was installed and run according to https://github.com/facebookresearch/esm. All predictions were run using the default settings with 10 recycles. All analysis was plotted using Matplotlib 3.5.3. The Pearson correlation coefficient (r) and P value were calculated using the SciPy package.

AutoDock Vina

We used AutoDock Vina 1.2.5 and the relevant scripts for input preparation from https://github.com/ccsb-scripps/AutoDock-Vina.

For ligand definition, we used the same mol2 file as in Rosetta design. Vina forcefield was used. The docking grid parameters were set to include the entire ligand-binding pocket. Default values were used for other settings.

Experimental materials and methods

HBC dyes. HBC599 was synthesized using a previously described synthetic route[29] (Supplementary Methods). HBC620 and HBC530 dyes were purchased from MedChemExpress (catalogue numbers HY-133520 and HY-D1373, respectively). HBC497 and HBC508 were synthesized using the synthetic route previously described.

Cloning and expression. The designer wFAPs and tmFAPs were encoded by synthetic DNA from GENEWIZ, subcloned into the pET-29b plasmid. For purification, a sequence encoding a His6-tag at the C terminus was added for all gene products. For *E. coli* imaging and directed evolution, we inserted the genes into a custom pBAD vector, encoding a construct wherein the C terminus of wFAP or tmFAP was linked to the N terminus of mTagBFP2 through a flexible linker, to monitor the protein expression level. A maltose-binding protein (MBP) domain was fused to the N terminus of tmFAPs, to enhance protein expression, in the constructs used for purification and directed evolution experiments. Both soluble and transmembrane proteins were expressed in Lemo (DE3) *E. coli* cells in LB medium, shaking at 220 r.p.m. The culture was grown at 37 °C until reaching an optical density at 600 nm (OD_{600nm}) of 0.6, and induced by 0.2 mM IPTG. The culture was then grown at 18 °C overnight. For directed evolution experiments, protein sequences were subcloned into the pBAD vector, with a C-terminal mTagBFP2. The constructs were expressed in BW27783 *E. coli* cells. The culture was grown at 37 °C in SOB medium until reaching an OD_{600nm} of 0.6, and induced by 0.0002% arabinose. wFAPs were expressed at 37 °C overnight, whereas tmFAPs were expressed at 22 °C for 3.5 h. Mammalian expressed genes were subcloned into a modified mTagBFP2 vector, in which a mouse immunoglobulin-κ signal peptide (METDTLLLWVLLLWVPGSTGD) and a neurexin transmembrane helix were added to the N terminus of MBP-fused FAP genes, to enhance plasma membrane localization. Point mutations were introduced using PCR and confirmed by DNA sequencing.

Directed evolution and single-site mutagenesis. For soluble-protein-directed evolution, a combinatorial library with approximately 3.2 million variants was constructed by encoding 5 residues in wFAP0 using the random codon NNK. DNA fragments encoding the library were generated by PCR. The fragments were ligated to the pBAD vector. The mutant library was then transformed into *E. coli* BW28873 cells using electroporation and subsequently cultured in SOB medium (Sigma) at 37 °C. Cells were induced for 20 h with 0.04% arabinose. Cells were then washed three times with TBS buffer and then incubated with HBC599 (1% dimethylsulfoxide (DMSO)) at room temperature for more than 10 min. Cells were sorted on the basis of fluorescence signal of HBC599 and mTagBFP2, using a flow cytometer (Melody, BD). The top 2–3% of the population was collected. The collected cells were then grown in SOB medium and subjected to the next round of flow cytometer screening. After three rounds of screening, enriched mutants were identified through monoclonal sequencing.

For evolution of tmFAP1, we used the same strain, vector, medium and cytometry setting as those for wFAP0 evolution. For FACS gating strategies, see Supplementary Fig. 2. A combinatorial library encoding approximately 1 million tmFAP1 mutants was constructed. The alteration options and the degenerate codons encoding them were: 12 all (NNK), 16 AGIRTV (RBA), 19 AV (GYA), 65 AS (KCA), 100 all (NNK), 146 AGIRTV (RBA), 149 all (NNK; Extended Data Fig. 3). The library was electroporated into *E. coli* BW27783 cells. The culture was grown to an OD_{600nm} of 0.6 at 37 °C with ampicillin, and induced by 0.0002% arabinose for 3.5 h. The culture was then spun down, gently washed twice with M9 medium, and incubated with HBC599 for at least 20 min. The top 1–2% of the cells were collected each round. The collected cells were grown in SOB medium without antibiotics for 1 h, before being plated on agar plates with ampicillin. Colonies were scraped from the plates the next day, and resuspended into liquid culture for the next round of evolution. Colonies from the evolution round 3 and round 4 were sequenced, to examine enrichment of mutants.

For single-site mutagenesis (Extended Data Fig. 9c,d), mutations were introduced into corresponding positions by PCR. The strain, vector, medium, cytometry program and sample preparation methods were the same as those used for directed evolution, unless otherwise specified. Both wFAP1.1 and tmFAP1.2 were induced for 3.5 h. All samples were incubated with 200 nM HBC599 for the same amount of time. A total of 3,000 events for each mutant were used for analysis. Flow cytometry data were collected by a BD FACSMelody Cell Sorter, and processed by FlowJo v9 and BD FACSChorus software. Single-site mutagenesis results were plotted using OriginPro 2023.

Fluorescence characterization. Dissociation constant (K_d), fluorescence spectra and extinction coefficient were measured using a Varioskan LUX Multimode Microplate Reader (Thermo). All fluorescence readings were measured in black 96-well microplates (Corning). Protein concentrations were estimated by measuring the absorbance at 280 nm (A_{280nm}) using a NanoPhotometer N60 (Implen). For K_d determination, purified protein at a series of concentrations was mixed with 50 nM HBCs. The final total volume for each condition was 100 µl, with 2% DMSO. Fluorescence reading at optimal excitation wavelength was then measured. The global dissociation constant was fitted using a custom equation by OriginPro 2023.

$$RFU_{net} = RFU_{observed} - RFU_{bg} = fold \times [protein{-}ligand] \quad (1)$$

$$[Protein{-}ligand] = 1/2 \times ([ligand_{total}] + [protein_{total}] + K_d - \sqrt{([ligand_{total}] + [protein_{total}] + K_d)^2 - 4 \times [protein_{total}] \times [ligand_{total}]}) \quad (2)$$

In equation (1), we assume that the activated fluorescence signal is linearly proportional to the protein–ligand complex concentration, and in equation (2), we assume that the association and dissociation between the protein and ligand follows the law of mass action. Fluorescence activation fold of FAPs was calculated using data observed in the K_d titration assay. We compared background fluorescence readings to the steady-state fluorescence readings, or to the highest observed readings (for weak binders whose steady state was not measured). Fluorescence spectra of the FAPs were measured with 2 µM HBCs and purified proteins in excess. A 200 µl volume of sample was used for each protein–HBC combination. Fluorescence reading was scanned using the optimal excitation and emission wavelength for each HBC–protein combination. For the tmFAP–HBC specificity assay (Extended Data Fig. 6j), 1 µM protein was mixed with 1 µM HBC for each combination, and the fluorescence reading at the optimal wavelength for each condition was measured.

All absorbance readings were measured in transparent 96-well microplates, using a Varioskan LUX Multimode Microplate Reader (Thermo). For extinction coefficient measurement, HBC at a series of concentrations was mixed with excess proteins. At least 95% of the HBCs were bound to proteins, as estimated on the basis of the K_d values. The mixture was incubated for at least 3 h at room temperature, before being added to a transparent 96-well microplate for absorbance measurement. We used the absorbance value at the absorbance peak of each HBC–protein combination. The values were subject to background subtraction using absorbance at 600 nm, at which HBCs have minimal absorbance, and were corrected for path length by measuring the absorbance of water at 900 nm and 975 nm. The extinction coefficient was calculated using the Beer–Lambert–Bouguer law,

by linear fitting of data points of at least four concentrations. The same method was used for measuring absorbance spectra of wFAP1.1 and free HBC599. For wFAP1.1, 5 μM HBC599 was mixed with excess protein. For free HBC599, 25 μM ligand was mixed with the buffer.

The absolute quantum yield was measured using the integrating sphere in the Edinburg FLS1000 Spectrometer. A 0.5 μM concentration of ligand was mixed with at least 2 μM proteins (1% DMSO), and incubated at 4 °C overnight in the dark. All samples were measured at room temperature with 495-nm excitation.

Protein purification. wFAPs were purified by Ni^{2+}-NTA affinity chromatography followed by size-exclusion chromatography. In detail, cells were resuspended and homogenized in lysis buffer containing 5 mM imidazole, 20 mM Tris-HCl pH 8.0 and 500 mM NaCl. After 24,000*g* centrifugation, the supernatant was incubated with Ni^{2+}-NTA beads. After the incubation, the beads were washed three times with wash buffer (20 mM imidazole, 20 mM Tris-HCl pH 8.0 and 500 mM NaCl), and eluted using elution buffer (100 mM imidazole, 20 mM Tris-HCl pH 8.0 and 500 mM NaCl). The eluted protein was then purified in TBS (pH 7.4) using a gel filtration column (Superdex 200 Increase 10/300 GL, GE Healthcare). Fractions of the target protein were collected on the basis of the A_{280nm} reading.

Anti-BRIL Fab was purified using protein A affinity chromatography, followed by size-exclusion chromatography. *E. coli* cells were grown in SOB medium until reaching an OD_{600nm} of approximately 0.6–0.8. Induction with 0.2 mM IPTG was performed, and the cells were cultured for an additional 20 h at 16 °C. The cells were then collected and resuspended in lysis buffer containing 0.5 M NaCl and 50 mM Tris at pH 7.4. The suspension was subjected to lysis using a high-pressure homogenizer, and the resulting lysate was centrifuged at 24,000*g* for 30 min. The supernatant was collected and loaded onto protein A resin, which was washed with wash buffer (0.5 M NaCl, 50 mM Tris, pH 7.4) at a flow rate of 1–2 ml min^{-1} in a cold room. The resin was washed with ten column volumes of wash buffer, and the Fab was eluted using 0.1 M acetic acid. Eluted fractions were collected into tubes containing 100 μl of 1 M Tris at pH 8.0 and 40 μl of 5 M NaCl, resulting in a final concentration of 0.1 M for both Tris and NaCl. The eluted protein was further purified by size-exclusion chromatography using a Superdex 200 Increase 10/300 GL column (GE Healthcare).

For tmFAP protein purification, *E. coli* cells were collected from 1-l culture, resuspended and homogenized in 30 ml lysis (25 mM Tris-HCl, pH 7.4, 150 mM NaCl) buffer. Cells were lysed using a high-pressure homogenizer. Cell debris was removed by centrifugation at 15,000*g* for 10 min. The supernatant was collected and ultracentrifuged at 25,000 r.p.m. for 1 h. The membrane fraction was dissolved with 1.5% *n*-octyl-β-D-glucopyranoside (OG; Anatracec) at 4 °C for at least 2 h, followed by 45 min of 15,000*g* centrifugation. The supernatant was loaded to Ni^{2+}-NTA beads, washed by 20 ml wash buffer (lysis buffer with 20 mM imidazole and 1.1% OG), and eluted by 10 ml elution buffer (wash buffer with additional 300 mM imidazole). The eluted protein was concentrated to 1 ml, and further purified by a Superdex 200 Increase 10/300 GL column (GE Healthcare). The buffer for gel filtration contained 25 mM Tris-HCl, pH 7.4, 150 mM NaCl and 1.1% OG. Fractions were collected according to A_{280nm} readings and SDS–polyacrylamide gel electrophoresis results.

The N-terminal MBP-tagged tmFAP–BRIL fusion protein, which includes a 3C cleavage site after MBP, was expressed and purified using a method similar to that for tmFAP, with some modifications. *E. coli* cells from a 3-l culture were collected, resuspended and homogenized in 30 ml lysis buffer containing 25 mM Tris-HCl (pH 7.4) and 150 mM NaCl. Cells were lysed using a high-pressure homogenizer, and cell debris was removed by centrifugation at 15,000*g* for 10 min. The supernatant was collected and subjected to ultracentrifugation at 25,000 r.p.m. for 1 h to isolate the membrane fraction. The membrane fraction was solubilized with 1.5% *n*-dodecyl-β-D-maltoside (Anatrace) at 4 °C for 2 h, followed by centrifugation at 15,000*g* for 45 min. The supernatant was then incubated with Ni^{2+}-NTA beads. The beads were washed with 20 ml lysis buffer containing 20 mM imidazole and 0.5% lauryl maltose neopentyl glycol (LMNG; Anatrace). Subsequently, the protein was eluted with elution buffer containing 200 mM imidazole and 0.5% LMNG. The eluted protein was concentrated to 1 ml and further purified using a Superdex 200 Increase 10/300 GL column (GE Healthcare) with TBS buffer containing 0.01% LMNG. The purified fractions were collected. The MBP-tag was removed by digesting the protein with 3C protease at 4 °C for 12 h, followed by a second round of gel filtration on the same column to remove the MBP-tag. Finally, the purified tmFAP–BRIL fusion protein was mixed with purified Fab and further purified using the Superdex 200 Increase 10/300 GL column. Peak fractions were collected and concentrated to approximately 7.6 mg ml^{-1} for cryo-EM sample preparation.

Circular dichroism. Circular dichroism (CD) data were collected in a 0.5 mm path-length cuvette from a Chirascan V100 Circular Dichroism spectrometer (Applied Photophysics). CD spectra of targets were measured from 180 to 280 nm in triplets and averaged. CD spectra scanning was applied at various temperatures from 20 °C to 95 °C. Temperature melts were conducted in 1 °C steps (heating rate of 1 °C min^{-1}) by measuring the signal at a wavelength of 222 nm. The concentration of protein measured in CD was 0.2 mg ml^{-1} in the buffer containing 20 mM Na_2HPO_4–KH_2PO_4 (pH 7.4), 150 mm NaCl.

Fluorescent protein thermal stability experiment. The protein was concentrated to 1 μM and then mixed with 1 μM of HBC599 (1% v/v DMSO) in the buffer containing 20 mM Na_2HPO_4–KH_2PO_4 at pH 7.4 and 150 mM NaCl. The mixture of protein and ligand was allowed to incubate overnight before conducting the thermal stability experiment. Next, the solution of protein and ligand was divided into qPCR tubes and placed into a Real-Time Quantitative PCR instrument (QuantStudio 5, Applied Biosystems). The fluorescence changes were measured using the melting curve technique at various temperatures. The temperature range for the experiment was from 20 °C to 95 °C and then from 95 °C to 20 °C, with a temperature change rate of 1 °C s^{-1} and a 10 s hold time for each measurement.

Crystallography. For crystallization, purified wFAP1.1 was concentrated to 12 mg ml^{-1}. Crystals were obtained by the hanging-drop vapour diffusion method at 18 °C. To set up a hanging drop, 0.8 μl of concentrated protein solution was mixed with 0.8 μl of crystallization solution containing 20% PEG1000, 100 mM sodium phosphate dibasic with citric acid pH 4.2 and 200 mM lithium sulfate. For wFAP1.1–HBC599 complex crystallization, wFAP1.1 was mixed with 2% (v/v) of 50 mM HBC599 after concentration. The crystals were obtained in the same condition as the apo protein.

Before X-ray diffraction experiments, crystals were soaked in the crystallization solutions containing an additional 20% v/v glycerol for cryoprotection. wFAP1.1 apo diffraction data were collected at the in-house single-crystal X-ray diffractometer at the Advanced Biomedical Technology Core Facility of Westlake University. The wFAP1.1–HBC599 complex diffraction data were collected at the Shanghai Synchrotron Radiation Facility beamline BL02U1. Data were processed and scaled using HKL2000 software[58].

Both the wFAP1.1 apo and wFAP1.1–HBC599 structures were determined by molecular replacement in PHASER[59] using the design model as the search model. The structural models were refined in PHENIX[60] and adjusted in COOT[39]. The model quality was checked by MolProbity[61]. The final refinement statistics are listed in Extended Data Table 1. All structure figures were prepared using PyMOL (https://www.pymol.org).

Cryo-EM data acquisition and processing. To prepare samples for the cryo-EM experiments, 3 µl of the purified tmFAP–BRIL–Fab complex proteins was applied onto a freshly glow-discharged holey carbon grid (Quantifoil, Au 300 mesh, R1.2/1.3). The grids were blotted for 4 s and then plunge frozen in liquid ethane cooled by liquid nitrogen using a Vitrobot Mark IV (Thermo Fisher Scientific) at 100% humidity and 8 °C. Cryo-EM data were collected at a nominal magnification of ×215,000 on a Titan Krios (Thermo Fisher Scientific) operating at 300 kV equipped with a Falcon4i detector and a Selectris X energy filter. Micrographs were recorded in a defocus range from −0.9 to −1.3 µm.

Cryo-EM data processing and model building. For tmFAP dataset 1, a total of 14,412 micrographs were collected and binned to a pixel size of 0.57 Å. Subsequently, contrast transfer function estimation was performed on the dose-weighted micrographs using CryoSPARC (v4.2.1)[62], and about 3,032,000 particles were picked using a Blob picker. After two-dimensional (2D) classification, about 610,000 particles were extracted. An initial 3D map was generated using ab initio reconstruction followed by non-uniform refinement. The total number of particles used for constructing this map was about 140,000, and the overall resolution was 3.26 Å. To improve EM density, an additional dataset (dataset 2) was collected. Templates were created using the aforementioned map. Subsequently, about 32,629,000 particles were picked using a template picker. Multiple rounds of 2D classification were conducted using seed-facilitated 2D classification with the ≈140,000 particles obtained previously as the seed. A total of about 2,692,000 particles were selected from 2D classification and further used for 3D ab initio reconstruction. Hetero refinement was used to classify the ≈1,123,000 particles obtained to achieve better density for the complex. Six different references were used, including five other suboptimal references. This classification resulted in a map containing 453,223 particles, which was further refined using non-uniform refinement to achieve a final resolution of 2.79 Å. The design model for tmFAP was refined against its corresponding density map using PHENIX[60], with secondary structure, Ramachandran and rotamer restraints applied. Iterative manual adjustments with COOT[39] were performed between rounds of PHENIX refinement. The cryo-EM data were processed by CryoSPARC 4.2.1, Coot-0.9.5 and Phenix-1.19.2.

Mammalian cell culture, transfection and fluorescence imaging. CHO-K1, hereafter referred to as CHO, cells were purchased from ATCC (number CCL-61TM, lot number 70052774) and cultured in Dulbecco's modified eagle medium with F-12 (Gibco, ThermoFisher), supplemented with 10% fetal bovine serum (Cellmax) and 50 U ml^{-1} of penicillin and streptomycin. The cell lines were frequently inspected by their morphological features and were not tested for mycoplasma contamination. The indicated plasmids were transfected into the cells using Lipofectamine 3000 Transfection Reagent (ThermoFisher), following the manufacturer's instructions. After 1 day of transfection, the cells were washed once with FluoroBrite DMEM (Gibco, ThermoFisher), which was then replaced with the indicated buffer containing 1% dye. Subsequently, the cells were incubated for 10 min and imaged using a Zeiss 980 confocal microscope.

Oocyte cell culture, RNA injection and imaging. The gene encoding tmFAP3 was linked to a C-terminal mTagBFP2 gene, and cloned into a DNA construct with *Xenopus* globin 5′-UTR sequence, 3′-UTR sequence and poly-A sequence. RNA was prepared by in vitro transcription using the T7 High Yield RNA Transcription Kit (Vazyme), following the manufacturer's instructions. All animal experiments were approved by the Westlake University Institutional Animal Care and Use Committee and conducted in accordance with the ARRIVE guidelines. Oocytes were collected from wild-type *Xenopus laevis* females (Nasco, catalogue number LM00535MX). Enzymatic defolliculation was performed using 3 mg ml^{-1} collagenase (Sigma). A 50 nl volume of 150 ng $µl^{-1}$ RNA was injected into each period-V *X. laevis* oocyte cell using Roboocyte2 (MCS). RNase-free water was injected into the negative control cells instead of RNA. Cells were then cultured in ND96 buffer (96 mM NaCl, 2 mM KCl, 1 mM $MgCl_2$, 1.8 mM $CaCl_2$, 5 mM HEPES, 40 mg l^{-1} sodium pyruvate and 100 mg l^{-1} geneticin (pH 7.4)) at 17 °C for 3 days. Before imaging, cells were moved to buffer containing 20 nM HBC599 and incubated for at least 1 h. Fluorescence was excited using a 405-nm and a 488-nm laser for mTagBFP2 and HBC599 channels, respectively, and recorded using a Zeiss 980 microscope.

Live-cell imaging in *E. coli*. *E. coli* cells expressing FAPs were spun down from liquid culture, washed twice with M9 medium, and incubated for at least 20 min with 200 nM HBC599 (1% DMSO) before imaging. Fluorescence was imaged using a Zeiss 980 microscope in Airyscan mode, with a 63× oil lens. A 405-nm and a 488-nm laser were used for mTagBFP2 and HBC599 signals, respectively. All imaging data were processed using ZEN Microscopy Software (Zeiss). Line scan analysis was plotted using OriginPro 2023.

Reporting summary

Further information on research design is available in the Nature Portfolio Reporting Summary linked to this article.

Data availability

The crystal structure models have been deposited in the Protein Data Bank (accession codes 8W6F and 8W6E). The cryo-EM maps have been deposited in the Electron Microscopy Data Bank under the accession code EMD-60929, and the associated model has been deposited in the Research Collaboratory for Structural Bioinformatics Protein Data Bank under the accession code 9IVK. All data are available in the paper or in the Supplementary Information. Source data are provided with this paper.

Code availability

Design models and all relevant scripts are available via Zenodo at https://doi.org/10.5281/zenodo.14196857 (ref. 63). Rosetta Modeling Suite 2019.47.61047 (https://www.rosettacommons.org/) is available to academic and non-commercial users for free. The source code for RIF docking is available via GitHub at https://github.com/rifdock/rifdock. ColabFold is available via GitHub at https://github.com/sokrypton/ColabFold. ColabDesign is available via GitHub at https://github.com/sokrypton/ColabDesign. AF2 weights can be downloaded from https://storage.googleapis.com/alphafold/alphafold_params_2022-12-06.tar. Source data are provided with this paper.

52. Dang, B. et al. De novo design of covalently constrained mesosize protein scaffolds with unique tertiary structures. *Proc. Natl Acad. Sci. USA* **114**, 10852–10857 (2017).
53. Hanwell, M. D. et al. Avogadro: an advanced semantic chemical editor, visualization, and analysis platform. *J. Cheminform.* **4**, 17 (2012).
54. O'Boyle, N. M. et al. Open Babel: an open chemical toolbox. *J. Cheminform.* **3**, 33 (2011).
55. Mirdita, M. et al. ColabFold: making protein folding accessible to all. *Nat. Methods* **19**, 679–682 (2022).
56. Baek, M. et al. Efficient and accurate prediction of protein structure using RoseTTAFold2. Preprint at *bioRxiv* https://doi.org/10.1101/2023.05.24.542179 (2023).
57. Lin, Z. et al. Evolutionary-scale prediction of atomic-level protein structure with a language model. *Science* **379**, 1123–1130 (2023).
58. Otwinowski, Z. & Minor, W. Processing of X-ray diffraction data collected in oscillation mode. *Methods Enzymol.* **276**, 307–326 (1997).
59. Storoni, L. C., McCoy, A. J. & Read, R. J. Likelihood-enhanced fast rotation functions. *Acta Crystallogr. D* **60**, 432–438 (2004).
60. Adams, P. D. et al. PHENIX: a comprehensive Python-based system for macromolecular structure solution. *Acta Crystallogr. D* **66**, 213–221 (2010).
61. Davis, I. W. et al. MolProbity: all-atom contacts and structure validation for proteins and nucleic acids. *Nucleic Acids Res.* **35**, W375–W383 (2007).
62. Punjani, A., Rubinstein, J. L., Fleet, D. J. & Brubaker, M. A. cryoSPARC: algorithms for rapid unsupervised cryo-EM structure determination. *Nat. Methods* **14**, 290–296 (2017).
63. Zhu, J. jz3216/tmFAP: initial release. *Zenodo* https://doi.org/10.5281/zenodo.14196857 (2024).
64. Goverde, C. A. et al. Computational design of soluble and functional membrane protein analogues. *Nature* **631**, 449–458 (2024).

Acknowledgements We acknowledge S. Fan and J. Wang for assistance in structure determination; J. Yu and Y. Zhang for providing the SYNJ2BP plasmid; K. D. Piatkevich for providing the modified mTagBFP2 plasmid; the cryo-EM facility, the flow cytometry facility and the microscopy facility at Westlake University for technical support; the Westlake University HPC Center for computation assistance; the Protein Characterization and Crystallography Facility of Westlake University for help in sample analysis; and Z. Chen from Instrumentation and Service Center for Molecular Sciences at Westlake University for the assistance in fluorescence quantum yield measurement. This work was financed by the Ministry of Science and Technology of the People's Republic of China (projects 2020YFA0909200 and 2022YFA1303700), the Zhejiang Provincial Natural Science Foundation of China (grant number LR23C050001), the Pioneer and Leading Goose R&D programmes of Zhejiang (grant numbers 2024SSYS0031 and 2024SSYS0029), the National Natural Science Foundation of China (projects 32430063 and 22137005) and a research grant from Westlake University.

Author contributions P.L. conceived and supervised the project; J.Z., M.L. and K.S. contributed equally to this work; J.Z. developed the computational method and designed the wFAPs and tmFAPs. J.Z. and M.L. performed the biochemical experiments and imaging. J.Z., M.L. and Y.W. performed directed evolution. M.L. prepared protein crystals and solved the crystal structure. L.Z. and R.G. synthesized HBC599 supervised by Q.H. M.L. prepared cryo-EM samples for data acquisition. K.S., J.S., D.M. and G.H. solved the EM structure of tmFAP. P.L., J.Z., M.L. and K.S. wrote the original draft and all authors participated in manuscript revision.

Competing interests J.Z., M.L. and P.L. are inventors on a provisional patent application (Application No. 202410300103.3) submitted by Westlake University for the functions of the wFAPs and tmFAPs described in this study. The remaining authors declare no competing interests.

Additional information

Supplementary information The online version contains supplementary material available at https://doi.org/10.1038/s41586-025-08598-8.

Correspondence and requests for materials should be addressed to Peilong Lu.

Peer review information *Nature* thanks the anonymous reviewers for their contribution to the peer review of this work. Peer reviewer reports are available.

a

Parametric scaffold generation	Generate 4-helix bundles using Crick equation
	Connect the helices into one chain by loop closure using Rosetta
RIFgen	Genenerate energetic favourable conformations of the ligand
	Search for rotamers interacting with the ligand by RIFgen
RIFdock	Use RIFdock to place the ligand to the center of the helical bindles. Require output with satisfied hydrogen bonds and minimal clashes.
Rosetta sequence design	Initialize the protein sequences by Rosetta fix-backbone sequence design. Select designs with binding pocket of high ddG and shape complementarity
	Rosetta flexible backbone design with the RIF residue-ligand interactions constrained
AF2 network	AF2 prediction of backbone coordinates for the designs
Update scaffold	Replace backbone with the AF2 prediction models
Update sequence	Rosetta sequence design with backbone constrained to the predicted coordinates
Update scaffold (to RIFdock)	Re-sample interactions by RIFdock against scaffolds generated during the sequence design stage
Update RIF residues	
Iterative sequence & scaffold update	Select designs with optimal binding pocket and whose struture is confidently recapitulated by AF2

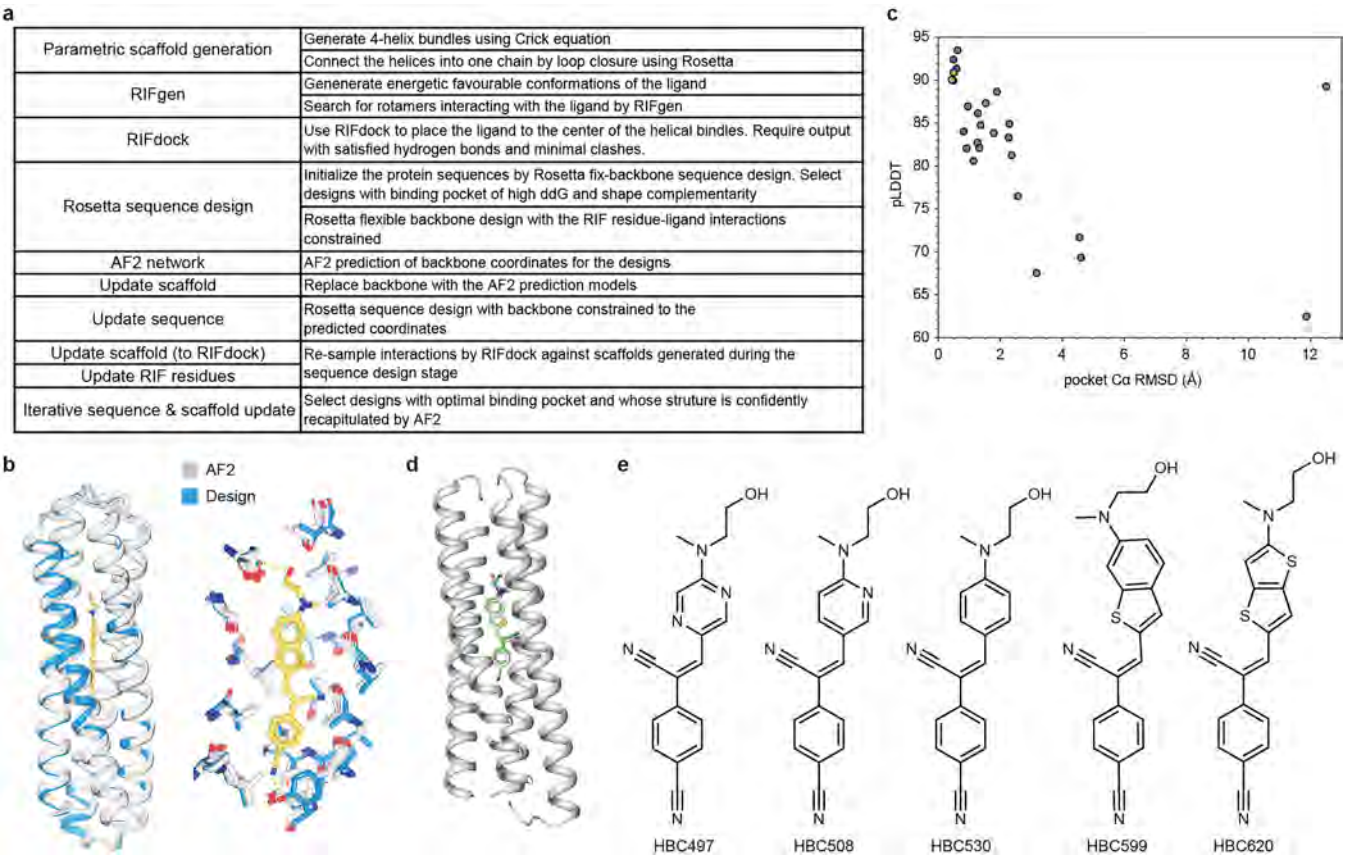

Extended Data Fig. 1 | De novo design of wFAPs. a, Detailed computational design steps of wFAPs. **b**, All five AF2 prediction models (white) aligned to wFAP0 design model (blue). Both the overall structure (left) and Cα coordinates of pocket residues (right) are highly consistent between the design and predictions. **c**, AF2 metrics of wFAPs designs, including the early designs and the revised designs. Overall pLDDT and pocket Cα RMSD to the design model are plotted for each experimentally tested wFAPs. Calculation is performed using all five AF2 models, and the averaged results are plotted for each design. wFAPs designed using the revised protocol (denoted by yellow dots for wFAP0 and wFAP1.3, the rest in blue) are significantly more consistent to AF2 prediction in the pocket region than those designed using the initial protocol (denoted by grey dots). **d**, HBC599 docked to the protein part of wFAP0 design model (white ribbon) by Autodock Vina. The overall binding mode in the top docking output (HBC599 in green) was highly consistent to that in the design model (white). **e**, Chemical structures of the HBC fluorophores[29] used in this study.

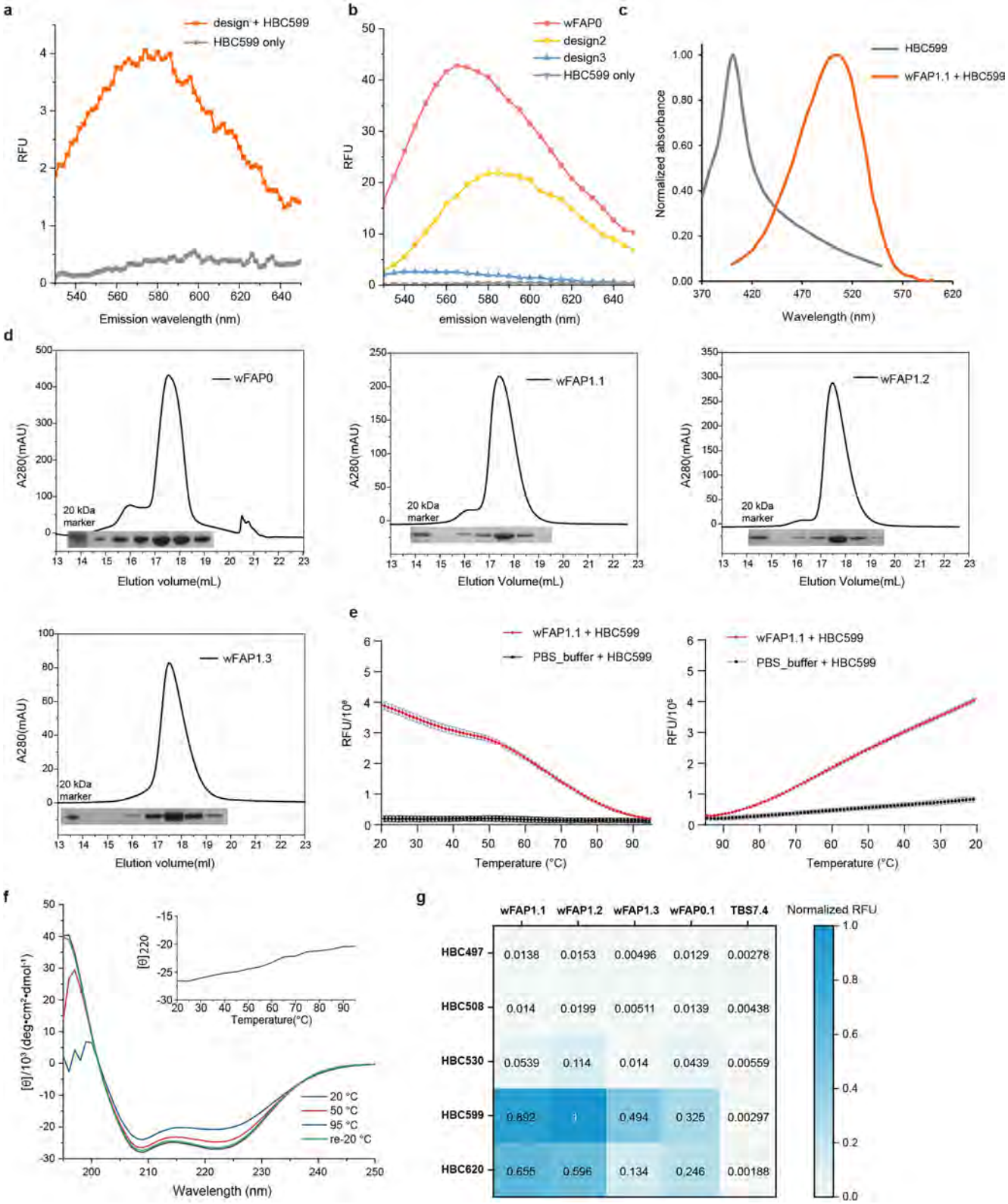

Extended Data Fig. 2 | See next page for caption.

Extended Data Fig. 2 | Purification and characterization of wFAPs. **a**, Fluorescence emission spectrum of 1 μM HBC599 with or without 10 μM of the best early design, excited at 495 nm. The design weakly activated fluorescence of HBC599 over the buffer (Tris-buffered saline (TBS, 20 mM Tris, pH 7.4, 150 mM NaCl)). **b**, Three designs demonstrated fluorescence activation for HBC599. Relative fluorescence intensity was measured at 1 μM HBC599 with 1 μM of each designer protein. **c**, Normalized UV-vis absorbance spectra of wFAP1.1-HBC599 complex (orange) and free HBC599 (gray). **d**, Representative gel filtration chromatography and SDS-PAGE of wFAP0, wFAP1.1, wFAP1.2 and wFAP1.3. All four proteins eluted as monomers at similar volume on size-exclusion chromatography (SEC). For gel source data, see Supplementary Fig. 1. At least two independent experiments were performed, yielding consistent outcomes. **e**, Fluorescence-temperature curves of the wFAP1.1-HBC599 complex (red) and free HBC599 (black) in the temperature-induced dissociation experiment. Fluorescence gradually diminished to the background level as the temperature rose to 95 °C, and recovered to the original level when the sample cooled down. The dissociation midpoint of wFAP1.1 was approximately 60 °C. Data from three independent samples are presented as mean ± SD. **f**, Far-ultraviolet CD spectra of apo wFAP1.1 at 20 °C (grey line), 50 °C (red line), 95 °C (blue line) and cooled back to 20 °C (green line). **g**, Ligand specificity of wFAPs. 1 μM protein or buffer (TBS, pH 7.4) was mixed with 1 μM HBC for each combination, and fluorescence reading at the excitation and emission maxima for each condition was measured. Readings were normalized against that of the best protein-ligand combination.

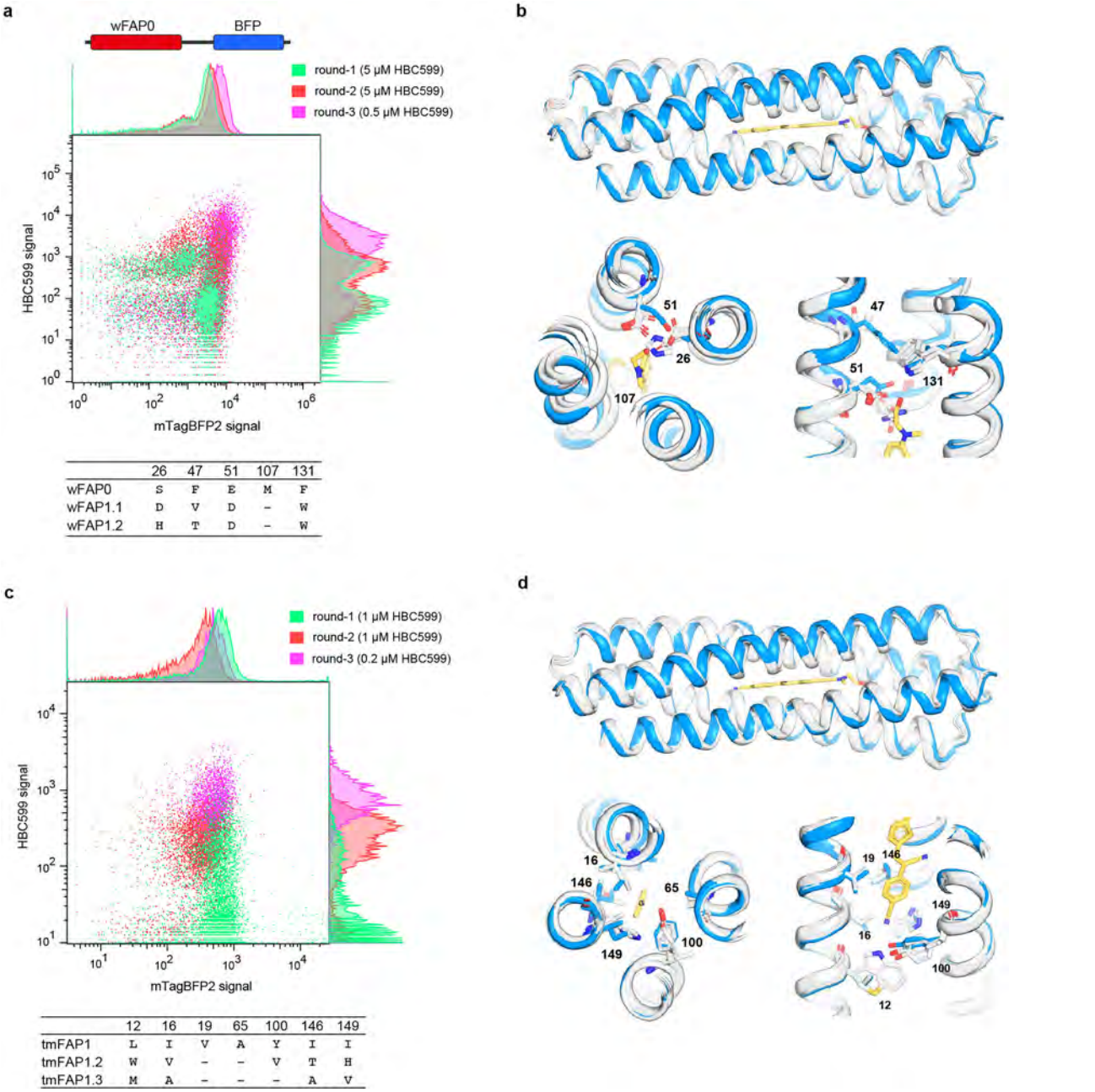

	26	47	51	107	131
wFAP0	S	F	E	M	F
wFAP1.1	D	V	D	–	W
wFAP1.2	H	T	D	–	W

	12	16	19	65	100	146	149
tmFAP1	L	I	V	A	Y	I	I
tmFAP1.2	W	V	–	–	V	T	H
tmFAP1.3	M	A	–	–	–	A	V

Extended Data Fig. 3 | Directed evolution of FAPs. a, Fluorescence-activated cell sorting (FACS) profile for each round of wFAP0 directed evolution. We constructed a combinatorial library with site-saturation mutation for five ligand-surrounding residues (in total 20^5 = 3,200,000 combinations). The selection comprised three rounds, with 5 μM HBC599 used for round 1-2, and 0.5 μM for round 3. mTagBFP2 was fused to the C-terminus of wFAP0 for monitoring of protein expression level. Upon completion of the final round of sorting, the sequences of individual clones were sequenced, leading to identification of two enriched variants, wFAP1.1 and wFAP1.2 (sequence at mutation sites listed at the bottom). For FACS gating strategies, see Supplementary Fig. 2. **b**, AF2 predictions of wFAP variants (white) aligned to wFAP0 design model (blue). Backbone structure of the ligand binding pocket remained unchanged after directed evolution. Indices of the mutated residues are labeled. **c**, FACS profile for each round of tmFAP1 directed evolution. We constructed a combinatorial library with mutations for seven ligand-interacting residues (in total ~1 million combinations). The selection comprised three rounds, with 1 μM HBC599 used for round 1-2, and 0.2 μM for round 3. mTagBFP2 was fused to the C-terminal of tmFAP for monitoring of protein expression level, and MBP fused to N-terminal for improving expression level. Upon completion of the final round of sorting, the sequences of individual clones were sequenced. Sequence at mutation sites listed at the bottom. For FACS gating strategies, see Supplementary Fig. 2. **d**, AF2 predictions of tmFAP variants (white) aligned to wFAP0 design model (blue). Indices of the mutated residues are labeled.

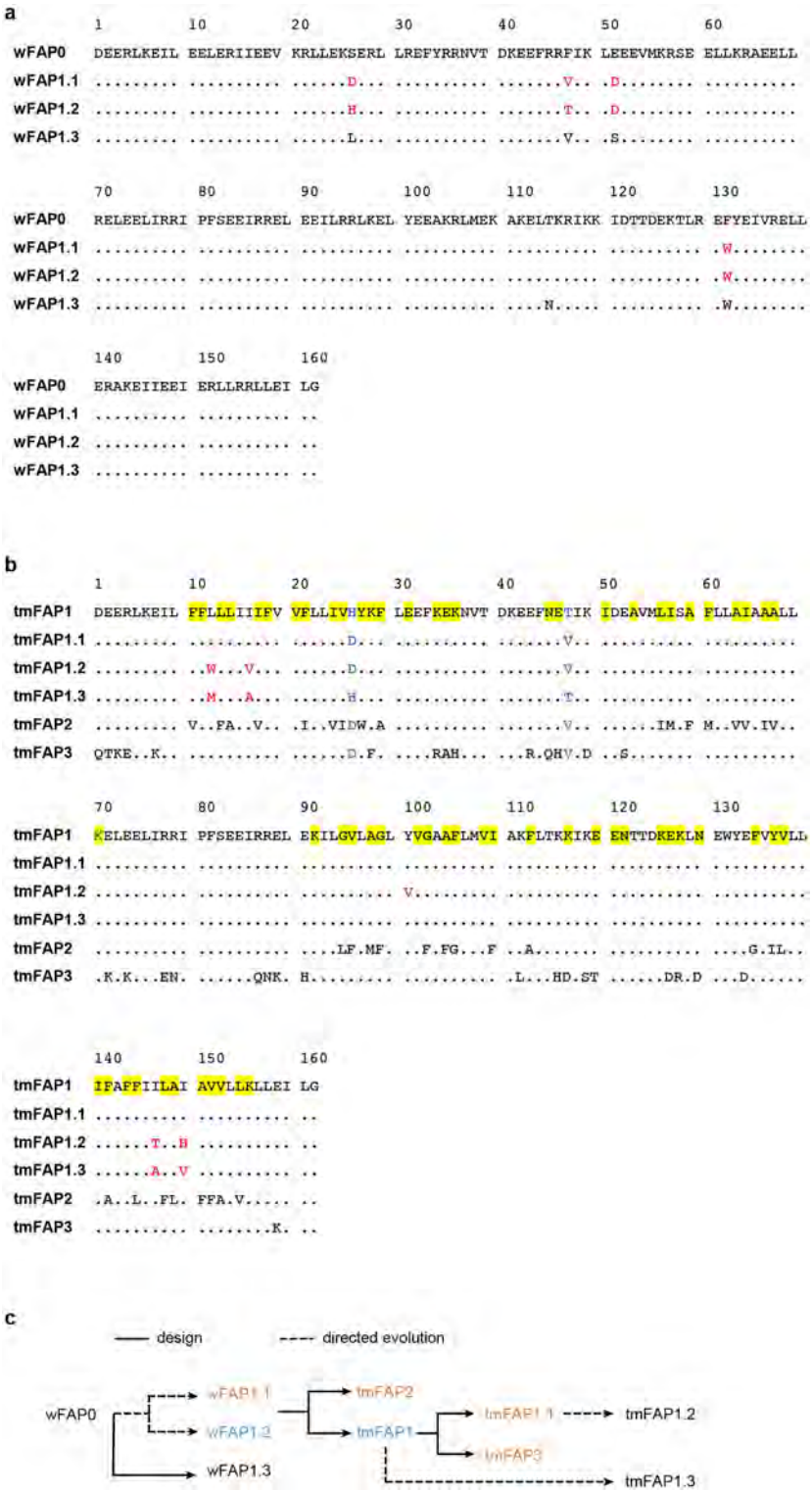

Extended Data Fig. 4 | Sequences of the designer FAPs. (**a**-**b**) Sequence alignment of wFAPs (**a**) and tmFAPs (**b**). Residues mutated through directed evolution are colored red. Unchanged residues are denoted by black dots. Residues changed during transmembrane span design (from wFAP1.1/1.2 to tmFAP1) are highlighted (yellow). Rational designed mutations are colored blue. (**c**) Sequence genesis of the designer FAPs. Arrows with solid lines denote sequence generation by design, while dashed lines denote sequence generation by directed evolution. Designs with the same color code (orange or blue) share the same set of residues in the ligand binding pocket.

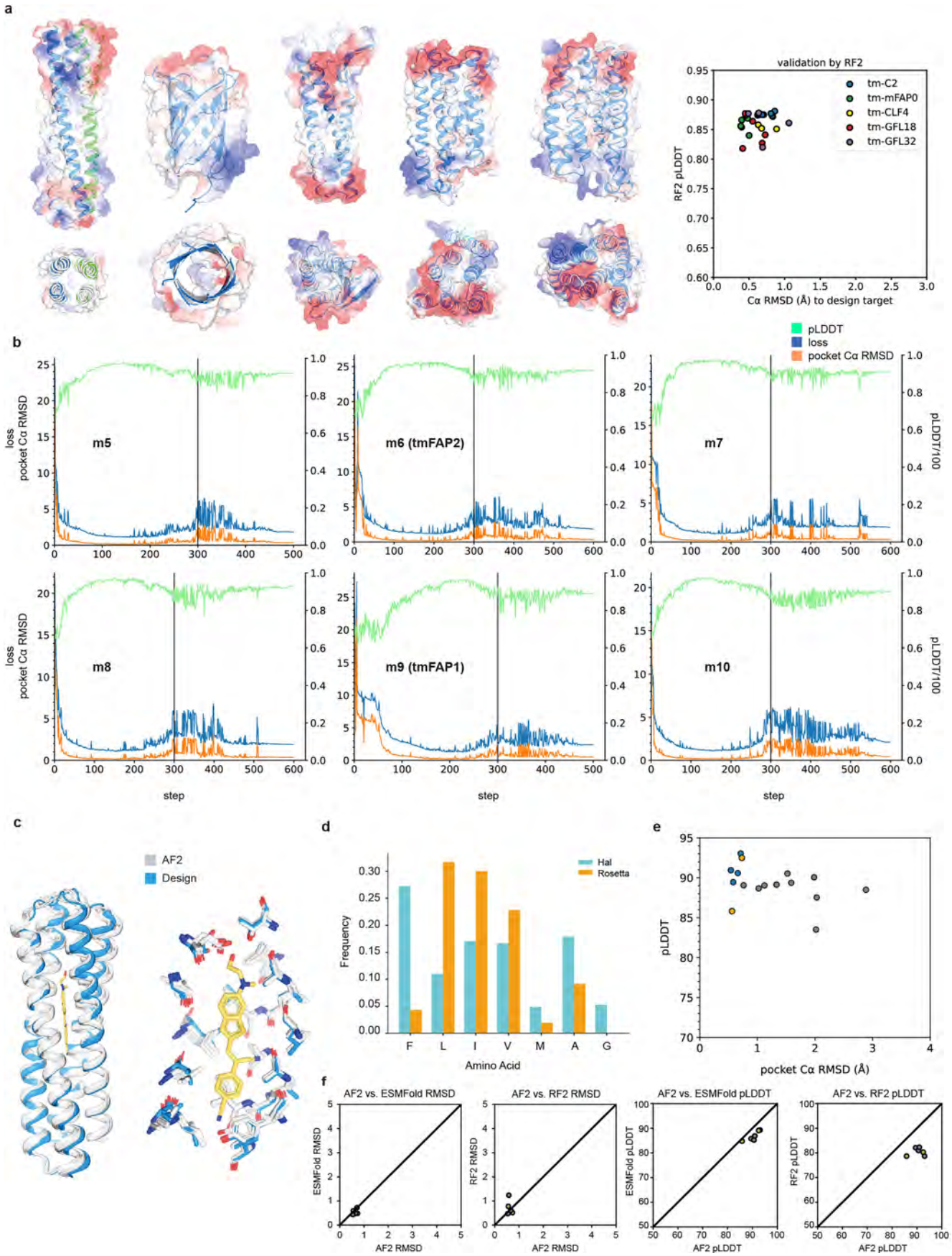

Extended Data Fig. 5 | See next page for caption.

Extended Data Fig. 5 | Design of the transmembrane span using deep networks hallucination. a, De novo transmembrane proteins designed by TM-span hallucination in addition to tmFAPs. Surface redesign was performed for five water-soluble precursor proteins in various topologies, including an alpha-helical homodimer (tm-C2)[2], a beta-barrel (tm-mFAP0)[5], a soluble analogue of Claudin (tm-CLF4) and two soluble analogues of GPCR (tm-GLF18, tm-GLF32)[64]. Left panel, the designs generated by TM-span hallucination. For designed sequences, see Supplementary Table 2. Model generated by RF2 validation (blue) was aligned to the water-soluble input (white). One representative design was shown for each target. Right panel, pLDDT and core residue Cα RMSD to the water-soluble input are plotted. **b**, Hallucination trajectories of the 6 tmFAP designs selected for experimental characterization, with Cα RMSD < 0.8 Å to the input wFAP template and pLDDT > 85. Loss sum (blue), pocket Cα RMSD (orange), and pLDDT (green) at each step are plotted. The vertical lines indicate the start of optimizing of one-hot encoded sequence at step 300. **c**, Prediction of all five AF2 models for tmFAP1 (white) aligned to the hallucination template, wFAP0 (blue). All ligand-interacting residues are highly consistent between the design template and the predicted models. **d**, Hallucination generated transmembrane span (cyan) has a different amino acid composition compared to that designed by the previous Rosetta protocol (orange). **e**, AF2 metrics of tmFAPs. Overall pLDDT and pocket Cα RMSD to the design model are plotted for each experimentally tested tmFAPs. Calculation is performed using all five AF2 models (for Rosetta designed sequences) or using the validation model (for hallucination generated sequences), and the averaged results are plotted for each design. tmFAPs designed by hallucination (denoted by colored dots—yellow for tmFAP1 and tmFAP2) are significantly more consistent to AF2 prediction in the pocket region than those designed by Rosetta (denoted by grey dots). **f**, RF2 and ESMFold were used as additional evaluation methods for tmFAPs, of which the results are overall consistent with AF2. Yellow dots represent tmFAP1 and tmFAP2.

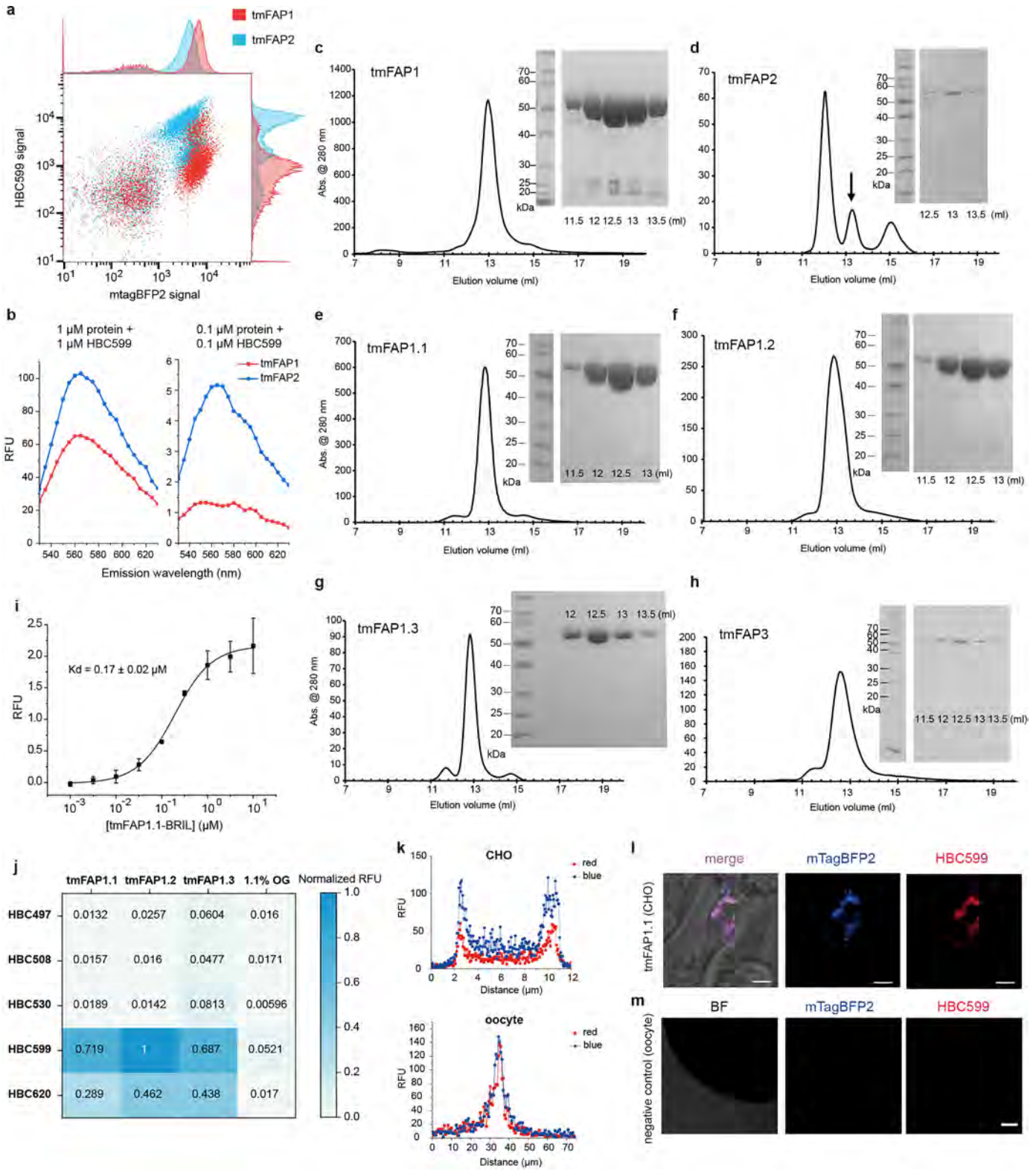

Extended Data Fig. 6 | See next page for caption.

Extended Data Fig. 6 | Purification and characterization of tmFAPs. (**a**-**b**), Both tmFAP1 and tmFAP2 were active for HBC599 when expressed in *E. coli* BW27783 cells (**a**, flow cytometry profiles) or purified in detergent solution (TBS, pH 7.4, 1.1% OG) (**b**). (**c**-**h**), Representative gel filtration chromatography and SDS-PAGE of tmFAP1, tmFAP2, tmFAP3, tmFAP1.1, tmFAP1.2, tmFAP1.3, and tmFAP3. All designs were fused with MBP at the N-terminus to improve expression level, and exhibited a similar elution volume on size-exclusion chromatography (SEC). However, it is worth noting that the expression level of tmFAP2 in *E. coli* cells was much lower than that of tmFAP1 variants. For gel source data, see Supplementary Fig. 1. At least two independent experiments were performed, yielding consistent outcomes. **i**, Fluorescence titration of tmFAP1.1-BRIL. Purified protein in detergent solution was titrated against 50 nM HBC599. Data from three independent experiments are presented as mean ± SD. **j**, Ligand specificity of tmFAPs. 1 μM protein or buffer (TBS, pH 7.4, 1.1% OG) was mixed with 1 μM HBC for each combination, and fluorescence reading at the excitation and emission maxima for each condition was measured. Readings were normalized against that of the best protein-ligand combination. (**k**-**m**), Fluorescence imaging of tmFAPs in eukaryotic cells. Line scans (in Fig. 5) across the membranes show substantial increase in fluorescence across the plasma membranes for tmFAP3 expressed in CHO cells (top panel) and *Xenopus* oocytes (bottom panel) in the presence of 20 nM HBC599. The BFP signal correlates with HBC599 signal very well. **l**, CHO cells expressing tmFAP1.1 in the presence of 20 nM HBC599. Scale bar is 10 μm. **m**, Control *Xenopus* oocytes cells injected with water in the presence of 20 nM HBC599. Scale bar is 100 μm. At least three independent experiments were performed (**l**-**m**), yielding consistent outcomes.

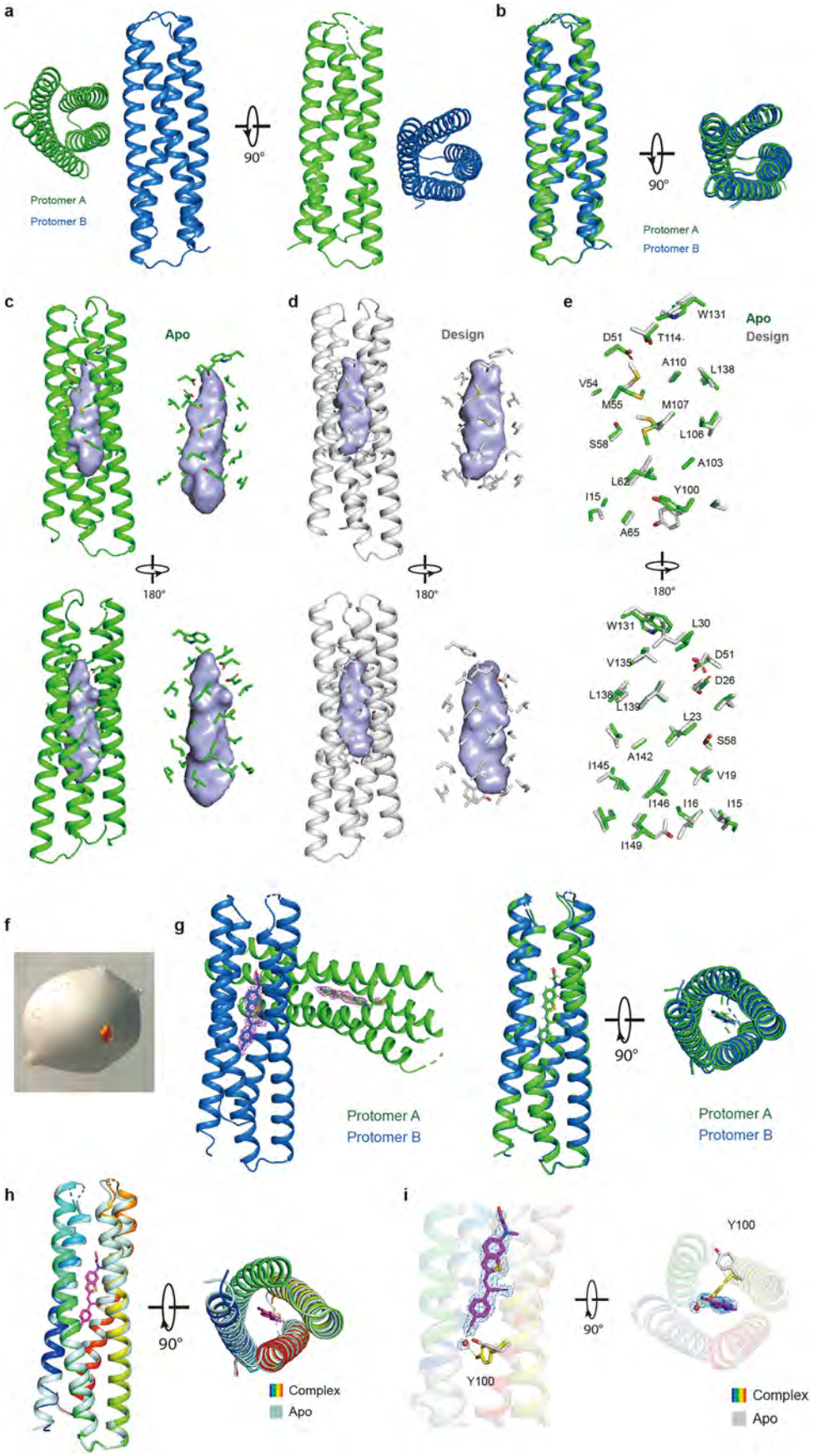

Extended Data Fig. 7 | See next page for caption.

Extended Data Fig. 7 | Crystal structures of wFAP1.1. a, Apo wFAP1.1 crystal structure comprises two molecules of wFAP1.1 in one asymmetric unit (green and blue). **b**, The conformations of the two wFAP1.1 biological units exhibit a high degree of similarity, as demonstrated by a Cα RMSD of 0.5 Å. (**c**-**d**), The ligand binding pocket, situated at the core of the helical bundle in the crystal structure (**c**), closely matches that of the design model (**d**). **e**, The residues defining the pocket in the crystal structure (green) align well with those in the design model (grey). **f**, Crystals of the wFAP1.1 in complex with HBC599 (scale bar: 100 µm). **g**, each asymmetric unit consists of two highly similar wFAP1.1 molecules. A single HBC599 molecule in its planar conformation is found nestled in the central pocket of each wFAP1.1 molecule, confirmed by unambiguous electron density as depicted in the omit map (contoured at 2.0σ). **h**, The crystal structures of wFAP1.1 in the ligand-bound form (rainbow) and the apo form (white) are nearly identical. **i**, Tyr 100 adopts distinct rotamers in the complex structure and the apo structure. The red sphere denotes the water molecule bridging HBC599 and Tyr 100 (omit map contoured at 2.0σ).

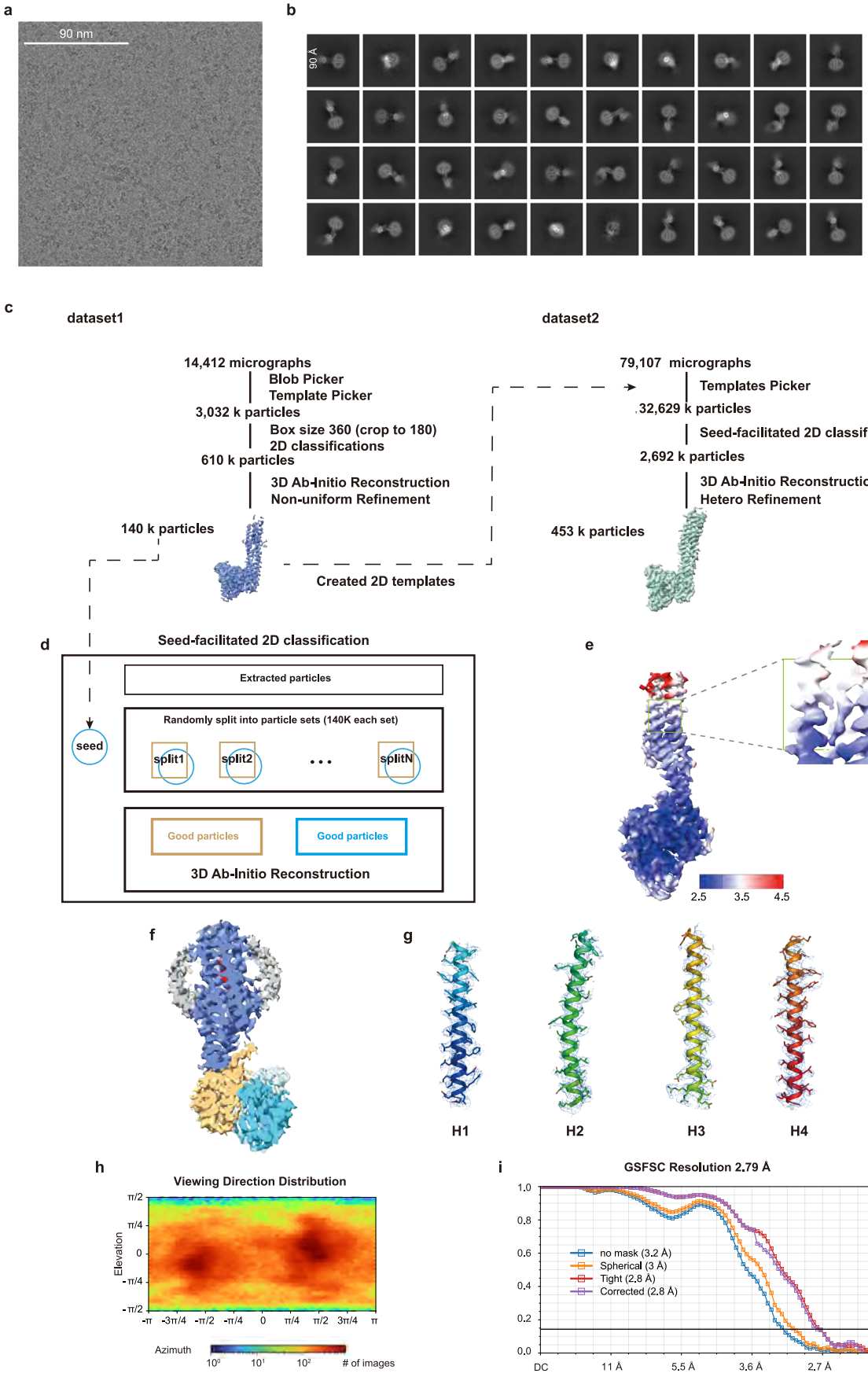

Extended Data Fig. 8 | See next page for caption.

Extended Data Fig. 8 | Single-particle cryo-EM image processing and analysis. a, Representative micrograph of tmFAP1.1-BRIL complexed with HBC599. Remaining micrographs produced consistent results. Scale bar is 90 nm. **b**, Representative 2D class averages. Remaining averages produced consistent results. Scale bars are 90 Å. (**c**-**d**), Flowchart for EM data processing (refer to Materials and Methods for details). **e**, Local resolution of the final cryo-EM map in Angstrom. **f**, Cryo-EM map of the surrounding detergents (grey). **g**, The cryo-EM density for the four helices of tmFAP1.1 (map contoured at 3.0σ). **h**, Angular distribution curve for the final refinement. **i**, Gold-standard Fourier Shell Correlation (GSFSC) curve for the final refinement.

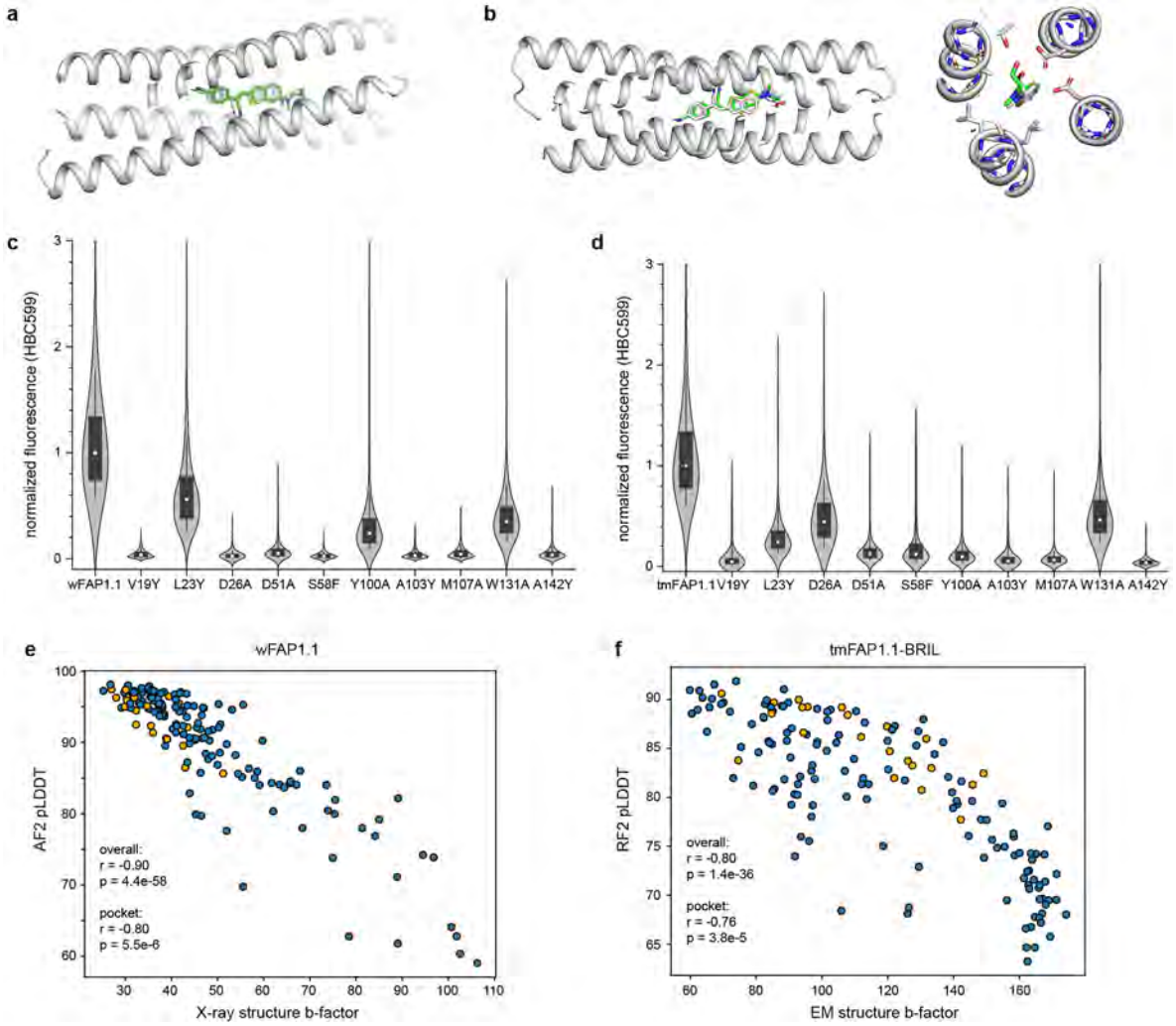

Extended Data Fig. 9 | Ligand binding in wFAP1.1 and tmFAP1.1 structures. **a**, HBC599 docked to the crystal structure of wFAP1.1 (white ribbon) by Autodock Vina. The top docking output is shown in green, highly consistent to that in the crystal structure (white). **b**, Potential binding mode for HBC620 to wFAP1.1. HBC620 was docked to the protein part of the wFAP1.1 crystal structure (white). The binding mode of HBC620 in the top output (green) closely resembled that of HBC599 (white). (**c**-**d**), Mutations introduced in the binding pockets of wFAP1.1 (**c**) and tmFAP1.1 (**d**) abolished or reduced the fluorescence activation, in agreement with the structures of wFAP1.1 and tmFAP1.1. *E. coli* cells expressing the mutants were analyzed by cytometry using the same method as directed evolution experiments. All samples were incubated with 200 nM HBC599 for the same amount of time. N = 3000 different cells of each mutant were used for analysis. The center dot denotes the median value. The upper and lower bounds of box denote the 25th and 75th of the data. Whiskers extended the range to the 10th to 90th percentile. (**e**-**f**), Correlation between pLDDT in structure prediction models and B-factor in experimental structures. Yellow dots denote pocket residues, while blue dots denote the remaining residues. The Pearson correlation coefficient (r) and p-value (p) are presented for all residues and pocket residues, respectively (Methods). Data plotted for **e**, wFAP1.1. **f**, transmembrane region of tmFAP-BRIL.

Extended Data Table 1 | Statistics of diffraction data collection and refinement

	wFAP1.1 (PDB ID:8W6F)	wFAP1.1-HBC599 (PDB ID: 8W6E)
Data collection		
Space group	P 1 21 1	P 1 21 1
Cell dimensions		
a, *b*, *c* (Å)	40.1, 92.4, 51.8	40.6, 91.9, 52.2
α, β, γ (°)	90, 108.1, 90	90, 107.8, 90
Resolution (Å)	50 - 2.35 (2.39 - 2.35)	30 - 2.10 (2.14 - 2.10)
R_{sym} or R_{merge}	0.084 (0.343)	0.127 (0.824)
$I / \sigma I$	20.2(4.3)	26 (1.3)
Completeness (%)	99.8 (100)	99.5 (95.1)
Redundancy	6.1 (6.1)	11.4 (5.5)
Refinement		
Resolution (Å)	25.42 - 2.35 (2.39- 2.35)	29.57 - 2.10 (2.14- 2.10)
No. reflections	14734	20877
R_{work} / R_{free}	0.222/0.244	0.218/0.244
No. atoms	2726	2872
Protein	2655	2755
Ligand/ion	-	86
Water	71	31
B-factors	42.68	51.96
Protein	42.63	51.89
Ligand/ion	-	49.04
Water	44.34	63.92
R.m.s. deviations		
Bond lengths (Å)	0.007	0.011
Bond angles (°)	1.09	1.49

Each diffraction dataset was collected from a single crystal. Values in parentheses are for the highest resolution shell. $R_{merge} = \Sigma_h \Sigma_i |I_{h,i} - I_h| / \Sigma_h \Sigma_i I_{h,i}$, where I_h is the mean intensity of the *i* observations of symmetry related reflections of *h*. $R = \Sigma |F_{obs} - F_{calc}| / \Sigma F_{obs}$, where F_{calc} is the calculated protein structure factor from the atomic model (R_{free} was calculated with 5% of the reflections selected).

Extended Data Table 2 | Cryo-EM data collection, refinement, and validation statistics

	tmFAP1.1-BRIL-HBC599 (EMDB-60929) (PDB 9IVK)
Data collection and processing	
Magnification	215,000
Voltage (kV)	300
Electron exposure (e–/Å^2)	50
Defocus range (μm)	-1.3 ~ -0.9
Pixel size (Å)	1.14
Symmetry imposed	C1
Initial particle images (no.)	35,661,789
Final particle images (no.)	453,223
Map resolution (Å)	2.79
FSC threshold	0.143
Map resolution range (Å)	2.554 ~ 42.526
Refinement	
Initial model used (PDB code)	design model
Model resolution (Å)	3.1
FSC threshold	0.5
Model resolution range (Å)	2.5 ~ 5
Map sharpening *B* factor (Å^2)	-82.7
Model composition	
Non-hydrogen atoms	4,077
Protein residues	507
Ligands	1
B factors (Å^2)	
Protein	89.65
Ligand	37.97
R.m.s. deviations	
Bond lengths (Å)	0.006
Bond angles (°)	0.869
Validation	
MolProbity score	1.51
Clashscore	9.67
Poor rotamers (%)	0.00
Ramachandran plot	
Favored (%)	98.00
Allowed (%)	2.00
Disallowed (%)	0

nature portfolio

Corresponding author(s): Peilong Lu

Last updated by author(s): 2024/11/22

Reporting Summary

Nature Portfolio wishes to improve the reproducibility of the work that we publish. This form provides structure for consistency and transparency in reporting. For further information on Nature Portfolio policies, see our Editorial Policies and the Editorial Policy Checklist.

Statistics

For all statistical analyses, confirm that the following items are present in the figure legend, table legend, main text, or Methods section.

n/a	Confirmed	
☐	☒	The exact sample size (*n*) for each experimental group/condition, given as a discrete number and unit of measurement
☐	☒	A statement on whether measurements were taken from distinct samples or whether the same sample was measured repeatedly
☒	☐	The statistical test(s) used AND whether they are one- or two-sided *Only common tests should be described solely by name; describe more complex techniques in the Methods section.*
☒	☐	A description of all covariates tested
☒	☐	A description of any assumptions or corrections, such as tests of normality and adjustment for multiple comparisons
☐	☒	A full description of the statistical parameters including central tendency (e.g. means) or other basic estimates (e.g. regression coefficient) AND variation (e.g. standard deviation) or associated estimates of uncertainty (e.g. confidence intervals)
☒	☐	For null hypothesis testing, the test statistic (e.g. *F*, *t*, *r*) with confidence intervals, effect sizes, degrees of freedom and *P* value noted *Give P values as exact values whenever suitable.*
☒	☐	For Bayesian analysis, information on the choice of priors and Markov chain Monte Carlo settings
☒	☐	For hierarchical and complex designs, identification of the appropriate level for tests and full reporting of outcomes
☐	☒	Estimates of effect sizes (e.g. Cohen's *d*, Pearson's *r*), indicating how they were calculated

Our web collection on statistics for biologists contains articles on many of the points above.

Software and code

Policy information about availability of computer code

Data collection	Rosetta Modeling Suit 2019.47.61047 (https://www.rosettacommons.org/) RifDock (https ://github.com/rifdock/rifdock, commit 9832eb409ad67781992010a0b6e861d99e75507a) ColabFold 1.3.0 (https://github.com/sokrypton/ColabFold) ColabDesign framework (https://github.com/sokrypton/ColabDesign; v 1.0.8 for tmFAP design; v 1.1.1 for the rest of membrane proteins) RFDiffusion 1.1.0 (https://github.com/RosettaCommons/RFdiffusion) ProteinMPNN (initial release version, https://github.com/dauparas/ProteinMPNN) BD FACSChorus v2.0 Zeiss ZEN Microscopy Software v3.5
Data analysis	Matplotlib 3.5.3; SciPy 1.14.1; OriginPro 2023; FlowJo 10.8.1; Zeiss ZEN Microscopy Software; HKL-2000-7.8; Coot-0.9.5; Phenix-1.19.2, CryoSPARC 4.2.1

For manuscripts utilizing custom algorithms or software that are central to the research but not yet described in published literature, software must be made available to editors and reviewers. We strongly encourage code deposition in a community repository (e.g. GitHub). See the Nature Portfolio guidelines for submitting code & software for further information.

Data

Policy information about availability of data

All manuscripts must include a data availability statement. This statement should provide the following information, where applicable:

- Accession codes, unique identifiers, or web links for publicly available datasets
- A description of any restrictions on data availability
- For clinical datasets or third party data, please ensure that the statement adheres to our policy

The crystal structure models have been deposited in the PDB (accession codes: 8W6E for wFAPI.1 complex structure; 8W6F for apo structure). The cryo-EM maps have been deposited in the Electron Microscopy Data Bank (EMDB) under accession number EMD-60929 and the associated model has been deposited in the RSCB Protein Data Bank (PDB) under accession number 91VK. All data are available in the paper or in the supplementary materials.

Research involving human participants, their data, or biological material

Policy information about studies with human participants or human data. See also policy information about sex, gender (identity/presentation), and sexual orientation and race, ethnicity and racism.

Reporting on sex and gender	N/A
Reporting on race, ethnicity, or other socially relevant groupings	N/A
Population characteristics	N/A
Recruitment	N/A
Ethics oversight	N/A

Note that full information on the approval of the study protocol must also be provided in the manuscript.

Field-specific reporting

Please select the one below that is the best fit for your research. If you are not sure, read the appropriate sections before making your selection.

☒ Life sciences ☐ Behavioural & social sciences ☐ Ecological, evolutionary & environmental sciences

For a reference copy of the document with all sections, see nature.com/documents/nr-reporting-summary-flat.pdf

Life sciences study design

All studies must disclose on these points even when the disclosure is negative.

Sample size	No statistical methods were used to pre-determine the sample size. The number of design ordered and tested was estimated based on success rate of previous results and experimental work load. Test number was increased until active design was obtained, or we conclude that the current design methods being suboptimal. For cryo-EM analysis, the number of micrographs recorded was determined by the availability of microscope time and sample quality. The cryo-EM data were collected until we obtained a high-resolution density map. For the mutants analyzed by cytometry, N=3000 cells of each mutant were used for analysis with statistical robustness.
Data exclusions	For cryo-EM analysis, micrographs with CTF fitting worse than 5-angstrom were discarded. Subsequent cryo-EM data processing only kept high-resolution and homogeneous particles to generate the final high-resolution maps. No data were excluded from the analyses.
Replication	Replication numbers are indicated in the legend of corresponding figures where applicable. All experiments were performed with at least two biological repeats and showed consistent results.
Randomization	Randomization was not applied to experiments in this study, as the results are not affected by sample allocation.
Blinding	Blinding was not used in this study because the subjective analysis was not needed. Each experiment was analyzed using consistent methods.

Reporting for specific materials, systems and methods

We require information from authors about some types of materials, experimental systems and methods used in many studies. Here, indicate whether each material, system or method listed is relevant to your study. If you are not sure if a list item applies to your research, read the appropriate section before selecting a response.

Materials & experimental systems

n/a	Involved in the study
☒	☐ Antibodies
☐	☒ Eukaryotic cell lines
☒	☐ Palaeontology and archaeology
☐	☒ Animals and other organisms
☒	☐ Clinical data
☒	☐ Dual use research of concern
☒	☐ Plants

Methods

n/a	Involved in the study
☒	☐ ChIP-seq
☐	☒ Flow cytometry
☒	☐ MRI-based neuroimaging

Eukaryotic cell lines

Policy information about cell lines and Sex and Gender in Research

Cell line source(s)	Chinese hamster ovary (CHO-K1, hereafter referred to as CHO) cells were purchased from ATCC (Number: CCL-61TM, Lot Number: 70052774)
Authentication	Cell lines were verified by the manufacturers' websites. The cell lines were frequently inspected by their morphological features.
Mycoplasma contamination	The cell lines were not tested for mycoplasma contamination.
Commonly misidentified lines (See ICLAC register)	None of the cell lines used is listed in the database of commonly misidentified cell lines maintained by ICLAC.

Animals and other research organisms

Policy information about studies involving animals; ARRIVE guidelines recommended for reporting animal research, and Sex and Gender in Research

Laboratory animals	Xenopus laevis females (Nasco, catalog # LM00535MX)
Wild animals	the study did not involve wild animals
Reporting on sex	The study used cocytes harvested from wild type Xenopus laevis females, and did not involve male animals.
Field-collected samples	the study did not involve field-collected samples
Ethics oversight	All animal experiments were approved by the Westlake University Institutional Animal Care and Use Committee. All experiments were conducted in accordance with relevant guidelines, and the study complied with the ARRIVE guidelines.

Note that full information on the approval of the study protocol must also be provided in the manuscript.

Plants

Seed stocks	N/A
Novel plant genotypes	N/A
Authentication	N/A

Flow Cytometry

Plots

Confirm that:

☒ The axis labels state the marker and fluorochrome used (e.g. CD4-FITC).

☒ The axis scales are clearly visible. Include numbers along axes only for bottom left plot of group (a 'group' is an analysis of identical markers).

☒ All plots are contour plots with outliers or pseudocolor plots.

☒ A numerical value for number of cells or percentage (with statistics) is provided.

Methodology

Sample preparation	E. coli BW27783 cells expressing wFAP or tmFAP was spun down, gently washed twice by M9 medium, and incubated with HBC599 for at least 10 min before flow cytometry.
Instrument	BD FACSMelody Cell Sorter
Software	BD FACSChorus Software for data collection FlowJo 10.8.1 and OriginPro 2023 for data analysis and plotting
Cell population abundance	The fraction collected during directed evolution was described in Extended Data Figure 3, Supplementary Information, and Methods section 'Directed evolution and single-site mutagenesis'
Gating strategy	FSC-A/SSC-A was used to gate E.coli cells; FSC-W/FCS-H and SSC-W/SSC-H was used to gate single cells. Gates for sorting was placed based on FACS profile of the previous round culture and the corresponding template variant, as illustrated in Extended Data Figure 3 and Supplementary Information.

☒ Tick this box to confirm that a figure exemplifying the gating strategy is provided in the Supplementary Information.